J. Fluid Mech. (2013), *vol.* 727, *pp.* 282–317. © Cambridge University Press 2013
doi:10.1017/jfm.2013.190

Boundary-layer noise induced by arrays of roughness elements

Qin Yang and Meng Wang†

Institute for Flow Physics and Control, Department of Aerospace and Mechanical Engineering, University of Notre Dame, Notre Dame, IN 46556, USA

(Received 23 March 2012; revised 22 March 2013; accepted 10 April 2013; first published online 20 June 2013)

Sound induced by arrays of 10×4 roughness elements in low-Mach-number turbulent boundary layers at $Re_\theta = 3065$ is studied with Lighthill's theory and large-eddy simulation. Three roughness fetches consisting of hemispheres, cuboids and short cylinders are considered. The roughness elements of different shapes have the same height of 0.124δ, the same element-to-element spacing of 0.727δ and the same flow blockage area. The acoustically compact roughness elements and their images in the wall radiate sound primarily as acoustic dipoles in the plane of wall. The dipole strength, orientation and spatial distribution show strong dependence on the roughness shape. Correlations between dipole sources associated with neighbouring elements are found to be small for these sparsely distributed roughness arrays. Correlations and coherence between roughness dipoles and surface pressure fluctuations are analysed, which reveals the importance of the impingement of upstream turbulence and surrounding vortical structures to dipole sound radiation, especially in the streamwise direction. For roughness shapes with sharp frontal edges, the edge-induced unsteady separation and reattachment also play important roles in sound generation. Large-scale turbulent structures in the boundary layer have a relatively low influence on roughness dipoles, except for the first row of elements.

Key words: aeroacoustics, boundary layers, turbulence simulation

1. Introduction

Noise generated by turbulent boundary layers due to surface roughness is of significant interest in naval and aeronautical applications. For underwater vehicles, continuous exposure to sea water inevitably causes surface roughness, and the vehicle's large surface-area-to-perimeter ratios make roughness noise particularly significant (Devenport *et al.* 2011). Such noise not only undermines the stealth performance of the vehicles but also obscures the weak signals their passive sonar systems aim to detect (Crighton *et al.* 1992). Roughness noise is also relevant to the design of low-noise airframes because it is a significant source of high-frequency cabin noise and airframe noise in clean configurations, when high-lift devices are not deployed (Liu & Dowling 2007).

It is well recognized that the noise from a turbulent boundary layer is generally weak if the surface is smooth and flat. The major acoustic source is the fluctuating

† Email address for correspondence: m.wang@nd.edu

https://doi.org/10.1017/jfm.2013.190 Published online by Cambridge University Press

Reynolds stress, which is of quadrupole nature based on Lighthill's aeroacoustic theory (Lighthill 1952). The surface pressure fluctuations, once thought to be a dipole sound source, are in reality specular images of the quadrupole sources (Powell 1960). Although the surface tangential forces due to viscous shear stress is a valid dipole sound source (Morfey 2003; Shariff & Wang 2005; Hu, Morfey & Sandham 2006), its magnitude is generally small in high-Reynolds-number boundary layers of practical interest. In contrast, a rough surface can induce large unsteady forces tangential to the wall, which can drastically enhance boundary-layer noise. From a theoretical standpoint, roughness noise is generated through a number of physical processes, which can be broadly categorized into two mechanisms (Glegg, Devenport & Grissom 2007; Yang & Wang 2009).

The first mechanism is diffraction of unsteady hydrodynamic pressure by the rough surface. This linear process facilitates the conversion of flow energy to acoustic energy, thereby altering the acoustic source character from quadrupoles to dipoles (Howe 1984, 1986). Based on Lighthill's theory (Lighthill 1952) with an approximate hard-wall Green's function for acoustically compact roughness elements, the dipole nature of roughness noise sources was revealed explicitly by Howe (1984, 1986). The diffraction mechanism plays a dominant role when roughness elements do not protrude beyond the buffer layer of a turbulent boundary layer, and the hydrodynamic flow field is not much affected by the roughness elements (Howe 1984, 1986, 1989).

The second mechanism for roughness noise is the modification of near-wall turbulence by surface roughness. When the roughness height extends beyond the buffer layer, the surface is hydraulically fully rough, which can distort the boundary-layer eddies and create new turbulence structures, thereby amplifying acoustic sources. Note that a hydraulically smooth surface can become hydraulically rough when the Reynolds number of a boundary layer grows larger, which causes the viscous sublayer and buffer layer to shrink in size relative to the boundary-layer thickness and roughness heights. The nonlinear interactions between flow and roughness elements provide a potentially stronger noise source mechanism than diffraction. Collectively, both mechanisms exert unsteady drag and side forces on the roughness elements which constitute acoustic dipole sources as described by Curle (1955).

Roughness noise has drawn attention from experimentalists since the early 1960s (Skudrzyk & Haddle 1960; Chanaud 1969; Cole 1980; Hersh 1983; Smol'yakov 2001). Grissom, Smith & Devenport (2006) reviewed the preceding experimental work and commented that only a handful of studies had been performed and their results did not paint a unified picture. In these early experiments, the focus was on establishing scaling laws for far-field acoustics in terms of boundary layer and roughness parameters. However, there were significant disagreements over suggested scaling laws, controlling parameters and the physical mechanisms behind the theories. The lack of understanding and predictive tools for roughness noise prompted a number of investigations in recent years, including the study of Liu, Dowling & Shin (2006, 2008) aimed at evaluating and modelling the contribution of roughness noise to airframe noise, and a concerted effort (Blake *et al.* 2008) consisting of theoretical (Glegg *et al.* 2007; Glegg & Devenport 2009), experimental (Anderson *et al.* 2007; Grissom, Devenport & Glegg 2007; Smith *et al.* 2008; Alexander *et al.* 2009, 2010; Alexander, Devenport & Glegg 2011, 2013; Devenport *et al.* 2010, 2011) and numerical (Yang & Wang 2008, 2009, 2010, 2011) investigations.

Liu & Dowling (2007) evaluated Howe's semi-empirical model (Howe 1998) using a number of different smooth wall pressure-spectrum theories with enhanced friction velocities and boundary-layer thicknesses to adjust for the presence of roughness, and

https://doi.org/10.1017/jfm.2013.190 Published online by Cambridge University Press

compared results with experimental measurements involving two flat plates roughened with hemispherical beads in an acoustically treated open jet wind tunnel. The results showed that all of the models predicted the frequency range of the acoustic spectral peak, but its magnitude was overpredicted, and the spectra decayed too slowly with frequency. Using the numerically integrated spectrum, they determined that the roughness height has a more significant impact on the far-field sound characteristics than the roughness density term in Howe's theory (Howe 1998). Liu *et al.* (2008) used the same predictive model developed by Liu & Dowling (2007) to estimate the sound pressure levels of the noise from two rough plates in an open jet. The resultant theoretical and measured source maps showed significant similarity, verifying the dipole nature of the sources.

In a recent theoretical development, Glegg & Devenport (2009) presented a 'unified theory' for roughness noise. Based on Lighthill's theory, the acoustic field is represented as a convolution integral of the surface pressure wavenumber spectrum and the wavenumber spectrum of the surface gradient, in which the acoustic diffraction acts as a wavenumber filter for the surface pressure spectrum. They applied this theory to several geometries, including Howe's hemispherical bosses, a discontinuous surface and a wavy wall. The hemispherical model yielded the same results of Howe (1998). The wavy wall results showed the possibility to explore low-wavenumber ranges of the wall pressure wavenumber spectrum by scattering waves of a desired frequency with a sinusoidal surface. Based on this idea, Devenport *et al.* (2010) proposed a new method for measuring the spectral characteristics of wall pressure fluctuations according to the far-field sound and validated it experimentally.

A series of experimental studies was performed in the Virginia Tech anechoic wall-jet facility. Roughness noise from short fetches of sandpaper roughness (Grissom *et al.* 2007; Smith *et al.* 2008; Devenport *et al.* 2011) as well as discrete roughness elements (Alexander *et al.* 2009, 2010, 2011) were measured. The sandpaper noise measurements were performed at a number of flow speeds and with various roughness sizes ranging from hydrodynamically smooth to fully rough. The background noise was sufficiently low to allow sound from even hydrodynamically smooth surfaces to be measured, which confirmed acoustic diffraction as a source mechanism. Based on the scattering theory of Glegg & Devenport (2009), a simple scaling relationship between wall pressure spectra and roughness noise spectra was established, which collapsed the measurement data at lower frequencies and confirmed the dipole nature of the acoustic source. Alexander *et al.* (2009) measured the sound generated from various discrete roughness elements including rocks, cubes and short cylinders, and investigated the effect of aerodynamic interaction among roughness elements on sound radiation. Little evidence of interaction was found except when elements were packed so closely as to be in touch with one another. A beamforming method to analyse source concentration and a least-squares method for estimating individual source strengths were applied for single cubic elements of various heights and arrays of hemispherical and cubic elements (Alexander *et al.* 2010, 2011). The results confirmed the existence of spanwise dipoles in addition to streamwise dipoles as suggested by the computational results of Yang & Wang (2009, 2010). The source distributions and orientation were in agreement with the computational findings. The frequency spectra of the streamwise and spanwise dipoles obtained from the least-squares technique also compared favourably with the computational predictions of Yang & Wang (2009, 2010) for both hemispherical and cuboidal elements.

Parallel to the aforementioned analytical and experimental studies, numerical investigations were performed using large-eddy simulation (LES) and Lighthill's

https://doi.org/10.1017/jfm.2013.190 Published online by Cambridge University Press

theory to provide physical insight into the near-wall flow physics that contributes to roughness noise generation. These studies involved flows over small, two-dimensional forward and backward steps (Ji & Wang 2010, 2012) and three-dimensional roughness elements (Yang & Wang 2008, 2009, 2010, 2011). Yang & Wang (2009) considered the sound from a single hemispherical roughness element and a pair of roughness elements in a boundary layer of $Re_\theta = 7500$. The roughness height is 3.6 % of the boundary-layer thickness, or 95 wall units. An acoustic formulation based on a half-space Green's function is developed, which shows dominance of compact dipole sources induced by unsteady drag and side forces and their images in the wall. Both diffraction and turbulence generation mechanisms were accounted for. This study resulted in a number of interesting, and in some cases surprising, discoveries: (a) dipole radiation in the spanwise direction, which has been overlooked in previous investigations, is of comparable strength or even stronger compared with that in the streamwise direction; (b) the dominant sound source is the unsteady surface pressure on the front part of roughness elements induced by incoming turbulent eddies and unsteady vortical structures formed around the elements; (c) vortex shedding is unimportant as a source of self-noise, in contrast to the earlier belief, but it significantly enhances sound radiation from downstream roughness elements.

In the present paper, the boundary-layer noise induced by arrays of sparsely distributed roughness elements is considered. This is a step further towards the understanding and prediction of the noise from realistic rough surfaces. The primary objective is to investigate sound characteristics, source mechanisms and hydrodynamic and acoustic interactions among roughness elements with consideration of the effect of the roughness shape. In particular, it is of interest to examine to what extent the conclusions drawn from the single- and double-element cases are valid for a large number of distributed elements. Based on the computational framework established by Yang & Wang (2009), a systematic investigation is performed for turbulent boundary layer flows over arrays of 10×4 hemispheres, cuboids and short cylinders. The discussions are primarily focused on hemispheres and cuboids because they represent two geometries in sharp contrast: one with a smooth surface and the other with sharp edges on the surface, which induce different flow dynamics. The statistical quantities examined include those associated with roughness dipoles and forces, surface pressure fluctuations and their correlations and coherence. The short-cylinder case provides additional insight into the effect of roughness shape and is presented briefly towards the end of the paper.

This paper is organized as follows: the computational methodology employed for flow and acoustics is described in § 2. Section 3 gives an overview of the flow characteristics and structures in the turbulent boundary layers over hemispherical, cuboidal and cylindrical roughness fetches. Section 4 provides a statistical description of roughness dipole sources in terms of their spatial distributions, frequency spectra, correlation and coherence, with a focus on hemispherical and cuboidal roughness fetches. Evidence of grid convergence of acoustic results and a comparison with experimental measurements are shown in § 5. Acoustic source mechanisms are explained in § 6 based on statistics of surface pressure fluctuations and their correlations and coherence with roughness dipoles. Section 7 summarizes the major results for the roughness fetch with short cylinders and compare them with the hemispherical and cuboidal fetches. Further discussions, with particular regard to the effects of Reynolds number and roughness height, are provided in § 8. Lastly, major conclusions from this study are summarized in § 9.

https://doi.org/10.1017/jfm.2013.190 Published online by Cambridge University Press

2. Computational approach and flow configuration

The computational method is described in detail by Yang & Wang (2009). It is a hybrid approach combining LES with Lighthill's aeroacoustic theory, which is computationally efficient and accurate for low-Mach-number flows (Wang, Freund & Lele 2006). For a roughness patch containing N discrete elements that are acoustically compact, the Lighthill equation can be solved using the half-space Green's function, and the acoustic pressure p_a at a far-field observer location $\boldsymbol{x}$ and time t can be approximated as (see Yang & Wang (2009) for the derivation)

$$p_a(\boldsymbol{x}, t) = \frac{1}{2\pi c_0} \sum_{n=1}^{N} \frac{R_\alpha^{(n)}}{R^{(n)2}} D_\alpha^{(n)} \left(t - \frac{R^{(n)}}{c_0} \right), \tag{2.1}$$

where c_0 is the ambient sound speed, $R = |\boldsymbol{x} - \boldsymbol{y}_c|$ is the distance between the observer and the central position $\boldsymbol{y}_c$ of the base of a roughness element on the plane wall, $R_i = x_i - y_{ci}$ is the ith component of $\boldsymbol{x} - \boldsymbol{y}_c$, the superscript (n) indicates quantity associated with the nth roughness element, and

$$D_i^{(n)}(t) = \frac{\mathrm{d}}{\mathrm{d}t} F_i^{(n)}(t) = \frac{\mathrm{d}}{\mathrm{d}t} \int_{S_r^{(n)}} n_j p_{ij}(\boldsymbol{y}, t)\, \mathrm{d}^2\boldsymbol{y} \tag{2.2}$$

are the acoustic dipole source functions that are equal to the time derivative of net unsteady forces $F_i^{(n)}(t)$ exerted on the fluid by the surface of the nth roughness element, $S_r^{(n)}$. In (2.2), n_j denotes the outward unit normal of the roughness surface, $p_{ij} = p\delta_{ij} - \tau_{ij}$ is the compressive stress tensor composed of pressure p and viscous stress tensor τ_{ij}, and $\boldsymbol{y}$ represents source coordinates. The repeated index α implies summation over 1 and 3 because only the net forces in the streamwise and spanwise directions contribute to dipole sound radiation. In the subsequent discussions, $D_i^{(n)}(t)$ and $F_i^{(n)}(t)$ are referred to as roughness dipole and roughness force, respectively, and the superscript (n) will be dropped for convenience.

Equation (2.1) can be interpreted as the surface-integral part of Curle's equation (Curle 1955) with account for the images of the roughness elements in the wall. The strengths of dipoles in the streamwise and spanwise directions are doubled due to constructive interference with their images, whereas the lift dipoles in the wall-normal direction interfere destructively with their images to form less efficient quadrupole sources. All quadrupole terms including surface and volume contributions have been neglected on the basis that they are $O(M)$ smaller than dipole terms at low free-stream Mach number M, and the dipole sources are approximately distributed on the flat surface because of acoustic compactness of the roughness elements. Note that the acoustic source region, or the roughness array, is not assumed acoustically compact, as the retarded time differences among acoustic waves from different roughness elements are fully accounted for by (2.1).

The preceding Lighthill formulation is particularly suited for the flow noise of roughness arrays considered here, because the low flow Mach number renders the roughness elements acoustically compact for practically all frequencies of interest, and the sparse distribution of compact roughness elements allows wave reflection by the surface to be reasonably approximated by specular reflection through the half-space Green's function. Some limitations of the acoustic formulation should be noted, however. Since the effect of turbulent-boundary-layer flow on wave propagation is neglected, accurate solutions can only be achieved for wavelengths that are long compared to the distance of propagation inside the boundary layer. The formulation is

https://doi.org/10.1017/jfm.2013.190 Published online by Cambridge University Press

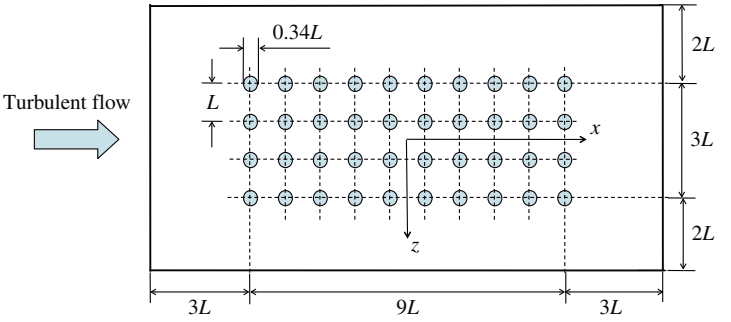


FIGURE 1. (Colour online) Schematic of a roughness fetch in the computational domain. The domain height is $4L$ in the wall-normal (y, out of the page) direction.

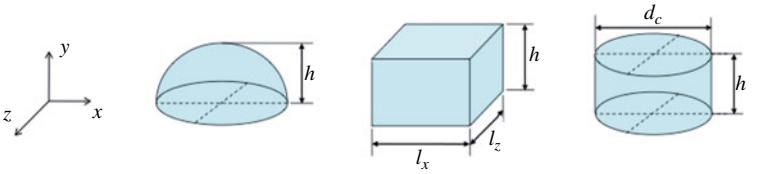


FIGURE 2. (Colour online) Hemispherical, cuboidal and cylindrical roughness elements, with $h = 0.17L$ and $l_x = l_z = d_c = 0.27L$.

inadequate for short wavelengths or propagation at grazing angles. Also note that wave interaction with roughness elements is not considered in the formulation, which again makes the acoustic solution less accurate at grazing angles.

The unsteady forces on the roughness elements, which are required to calculate acoustic dipole sources in (2.2), are obtained using LES. Simulations are carried out using a finite volume, unstructured-mesh LES code developed at Stanford University (Mahesh, Constantinescu & Moin 2004). The cell-based numerical scheme is energy-conservative and low-dissipative, allowing an accurate representation of a wide range of turbulence scales that are relevant to sound generation. The code is second-order accurate in both time and space. It employs a fully implicit, fractional-step time integration for momentum equation and an algebraic multigrid Poisson solver for pressure. The effect of subgrid-scale motions on the resolved scales is modelled by the dynamic Smagorinsky model. In the acoustic calculation the contribution of the subgrid-scale stress to the Lighthill stress as a quadrupole sound source is neglected along with all resolved quadrupole sources, but its contribution to the unsteady surface pressure and thereby roughness dipole sources at resolved scales is accounted for in the LES.

The flow configuration and computational domain are shown schematically in figures 1 and 2. Three roughness fetches, consisting of hemispherical, cuboidal and cylindrical roughness elements, respectively, are considered. The roughness elements are arranged deterministically in 10 rows in the streamwise direction and 4 columns in the spanwise direction. They are evenly spaced in both directions with a centre-to-centre separation of $L = 5.88h$, where h is the roughness height. The two lateral dimensions of the cuboids are $l_x = l_z = 1.59h$ and the cylinder diameter is $d_c = 1.59h$, which are chosen to match the flow blockage area of the

https://doi.org/10.1017/jfm.2013.190 Published online by Cambridge University Press

hemisphere. The boundary-layer thickness at the inlet, which is $3L$ upstream of the centre of the first row of elements, is $\delta = 1.375L$. The momentum-thickness-based Reynolds number is $Re_\theta = U_\infty \theta/\nu = 3065$, which corresponds to a friction Reynolds number of $Re_\tau = u_\tau \delta/\nu = 1307$. Relative to the inlet boundary-layer properties, the roughness height is $h = 0.124\delta$, or $h^+ = 168$ in wall units, which renders the surfaces hydraulically rough and therefore creates strong modifications of near-wall turbulence. The computational domain size is $15L$ in the streamwise direction, $7L$ in the spanwise direction, and $4L$ in the wall-normal direction (normal to the page), as shown in figure 1. The centre of the roughness fetches coincides with the centre of the bottom wall, which serves as the origin of the coordinate system. The boundary conditions consist of a stress-free condition on the top boundary, periodic condition in the spanwise direction, convective condition at the outlet, no-slip condition on the rough surface and turbulent inflow at the inlet. The time-dependent turbulent inflow data are generated from a separate LES of a smooth-wall boundary layer using the rescale and recycle technique of Lund, Wu & Squires (1998).

The number of grid cells employed is approximately 4×10^7 in each case. The grid distribution is very dense near the roughness elements, with the first off-wall grid spacing approximately equal to two wall units in the wall-normal direction. Away from the roughness elements, the grid is coarsened gradually to that with a typical boundary-layer resolution: $\Delta x^+ \approx 50$, $\Delta z^+ \approx 25$ and $\Delta y^+_{min} \approx 2$. The accuracy of the current LES approach and grid resolution requirement were established by Yang & Wang (2009) by comparisons with experimental measurements of velocity and Reynolds stress profiles behind a single hemisphere. Further validation is provided in § 5 based on a grid-sensitivity study of the acoustic source spectra and a comparison with experimentally measured roughness force spectra. The time step size is determined based on a maximum Courant-Friedrichs-Lewy (CFL) number of 1.5. Flow and acoustic statistics are collected over a period of approximately $240L/U_\infty$, or 16 flow-through times based on the domain length. To improve statistical convergence, two separate simulations with turbulence inflow data shifted in the spanwise direction by $3.5L$, or one half of the spanwise domain size, were performed for the hemispherical and cylindrical fetches. The cuboidal case was found to converge more slowly due to wider wakes and larger wake structures, and therefore four simulations with a consecutive spanwise shift of inflow data by $1.75L$ were performed. This created two (four for the cuboidal fetch) statistical samples as the roughness fetches encounter different turbulence structures from upstream. Statistical averaging is performed over the two (four for the cuboidal fetch) simulations, in time, and over the appropriate rows and columns of roughness elements as specified below.

3. Flow field and structures

Global views of flow fields in terms of the instantaneous streamwise velocity are shown in figure 3 in the x–y plane cutting through the centre of the second column of the hemispherical, cuboidal and cylindrical roughness elements. A wide range of flow scales are present, all of which can potentially contribute to sound generation. The roughness elements create intense turbulence structures and complex interstitial flows. This figure also shows the different flow structures encountered by the first row of roughness elements as compared with those encountered by the subsequent rows. The lead row interacts with turbulent eddies in a smooth-wall boundary layer whereas the subsequent rows are immersed in the turbulent wakes with more intense vertical

https://doi.org/10.1017/jfm.2013.190 Published online by Cambridge University Press

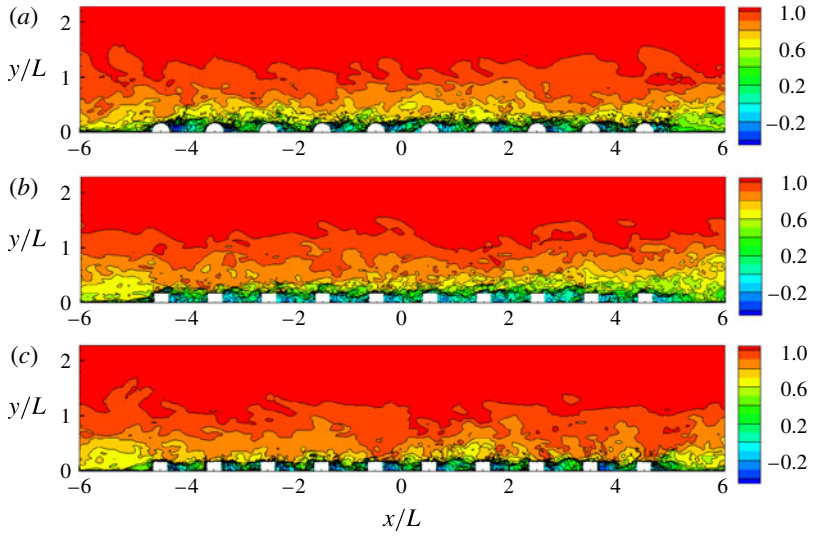


FIGURE 3. Isocontours of instantaneous streamwise velocity u/U_∞ in plane $z = -0.5L$ (cutting through the centre of the second column of roughness elements) in (*a*) hemispherical, (*b*) cuboidal and (*c*) cylindrical fetches.

structures. This indicates that the flow and acoustic sources will undergo a streamwise evolution in the roughness fetch before they become fully developed.

Figure 4 displays contours of the time-averaged streamwise velocity in the same x–y plane for all three roughness fetches, with only the first five elements in the second column plotted. It shows clearly the streamwise development of the rough-wall boundary layer and the size and shape of recirculation zones behind the roughness elements. The recirculation bubble is stronger and larger behind the lead row, and for cuboids and cylinders, small recirculation zones are visible above the upper surface near the leading edge. Small recirculation bubbles also exist in front of the roughness elements near the base, which correspond to the heads of horseshoe vortices formed around the elements. These horseshoe vortices can be visualized in figure 5, which shows the surface vorticity magnitude. They are most coherent for the lead row of roughness elements. In subsequent rows they are broken down by the turbulent wakes from upstream and become less coherent. The horseshoe vortices play a role in sound generation as will be illustrated later.

To better illustrate flow structures induced by roughness elements, instantaneous vorticity magnitudes in the plane $y = h/2$ are shown in figure 6 for rows 1 to 5 and columns 1 and 2. The vortical structures created around the three types of roughness elements exhibit noticeable differences. For hemispheres, flow separation occurs at approximately 90° from the upstream direction, creating a more confined wake region than both cuboids and short cylinders. For cuboids, flow separation first occurs at the front edges and generates intense vortical structures along both sides, creating wakes with a wider spread in the spanwise direction, while the back surfaces are shielded from strong vortical motions. Cylinders also create wakes with a relatively wide spread. For all three roughness shapes, the vortical structures do not exhibit an appreciable difference between inner columns and outer columns among the four columns in the roughness fetch. This observation implies that there is no strong

https://doi.org/10.1017/jfm.2013.190 Published online by Cambridge University Press

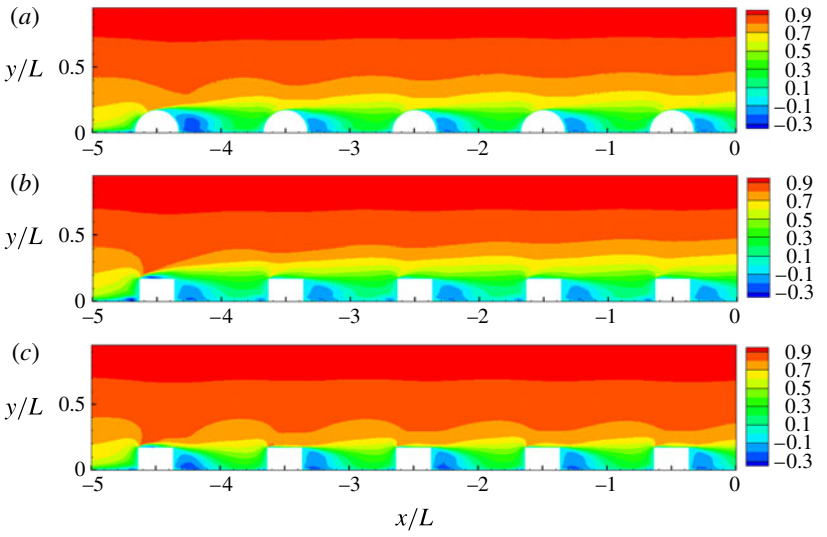


FIGURE 4. Isocontours of time-averaged streamwise velocity U/U_∞ in plane $z = -0.5L$ (cutting through the centre of the second column of roughness elements) in (*a*) hemispherical, (*b*) cuboidal and (*c*) cylindrical roughness fetches. Only the first five elements are shown.

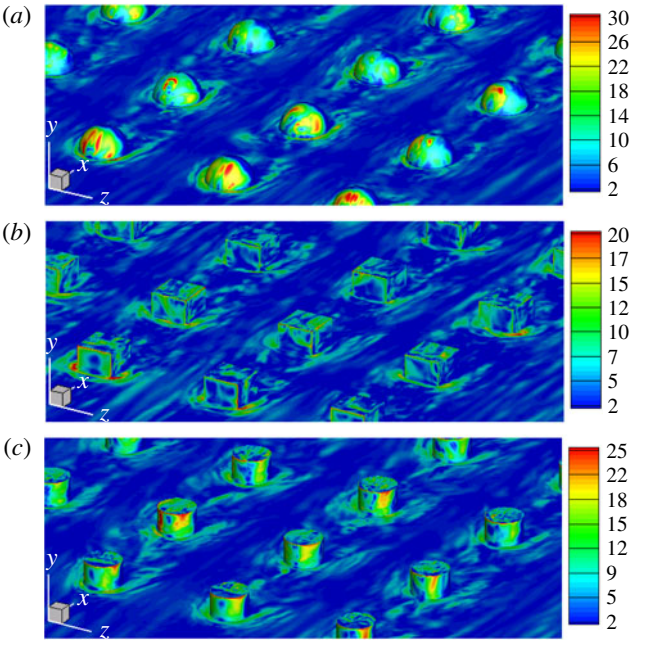


FIGURE 5. Isocontours of instantaneous vorticity magnitude $\omega h/U_\infty$ on the surface of the (*a*) hemispherical, (*b*) cuboidal and (*c*) cylindrical fetches for rows 1 to 4.

hydrodynamic interaction between columns of roughness elements in these sparsely arranged roughness arrays.

https://doi.org/10.1017/jfm.2013.190 Published online by Cambridge University Press

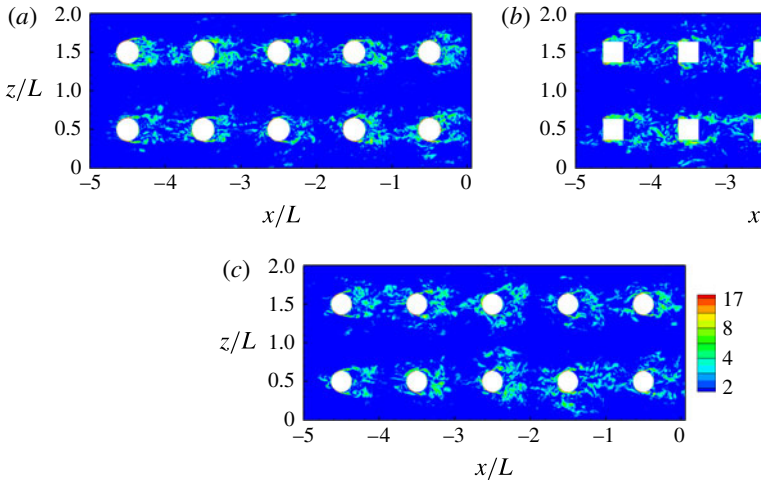


FIGURE 6. Isocontours of instantaneous vorticity magnitude $\omega h/U_\infty$ in plane $y = h/2$ (cutting through half the roughness height) in (*a*) hemispherical, (*b*) cuboidal and (*c*) cylindrical roughness fetches for rows 1 to 5 and columns 1 and 2. Contour levels are distributed logarithmically.

More discussions of the velocity and pressure characteristics are presented in § 6 in connection with acoustic source mechanisms.

4. Roughness dipoles sources

For clarity of presentation, the acoustic analysis in this section as well as in §§ 5 and 6 is focused on the hemispherical and cuboidal roughness fetches. These two types of elements are representative of geometries with smooth surfaces and with sharp edges, respectively, which induce different flow dynamics and acoustic source processes. The cylindrical elements share geometric features of both hemispheres and cuboids, and their acoustic characteristics mostly lie in between. Furthermore, it is found that a fully developed state is not reached within 10 rows with cylindrical elements, making a quantitative comparison with the other two roughness types difficult. The major results for cylindrical elements are therefore presented separately in § 7.

4.1. *Dipole source distributions*

As explained in § 2, each roughness element radiates sound as a dipole in the plane of the wall, which can be decomposed in the streamwise and spanwise directions. Figure 7 shows the variations of the root mean square (r.m.s.) of roughness dipole source strengths, defined in (2.2), associated with all roughness elements in hemispherical and cuboidal roughness fetches. In this plot, each symbol corresponds to one element whose streamwise position is indicated by the x-coordinate. Each line connecting the symbols represents a column, with solid and dashed lines denoting streamwise and spanwise components of dipole sources, respectively. Considerable variations of dipole strengths are exhibited along the streamwise direction as flow enters the roughness fetch. For hemispheres, the first row of elements emits the weakest sound and the second row emits the strongest sound among all rows. For cuboids, the first and second rows are the strongest sources and the subsequent rows emit sound with a decaying strength. The spanwise (column-to-column) variation of

https://doi.org/10.1017/jfm.2013.190 Published online by Cambridge University Press

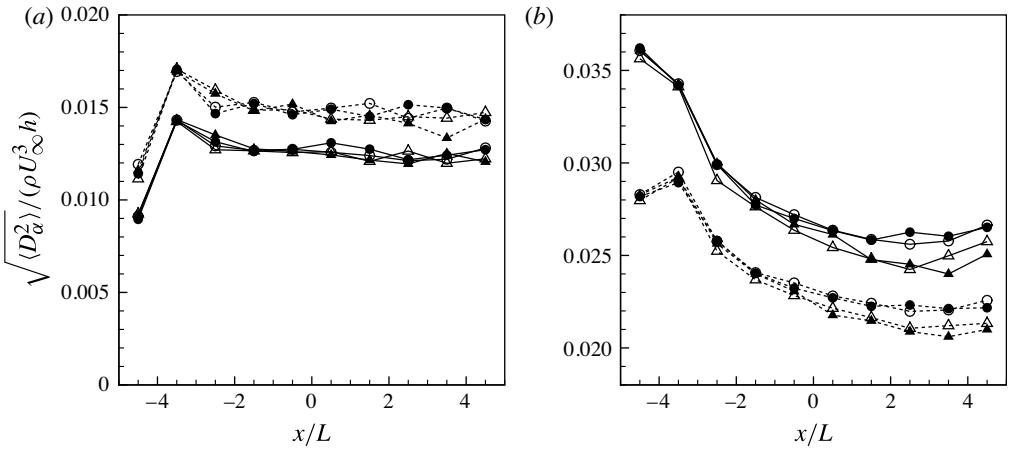


FIGURE 7. Root mean square of roughness dipole functions for (*a*) hemispherical and (*b*) cuboidal fetches. Each symbol corresponds to one roughness element: ——, streamwise component; - - - -, spanwise component. ○, first column; △, second column; ▲, third column; ●, fourth column.

dipole strengths is relatively small and not distinguishable from statistical convergence errors, except for the last 5 rows of cuboids. For these 5 rows a small difference between inner and outer columns is noted, indicating a small but non-negligible hydrodynamic interference among columns of cuboidal elements. The difference between the two inner columns or the two outer columns is representative of statistical errors because they are statistically equivalent. In the subsequent analysis, the small differences between inner and outer columns are neglected, so that a spanwise averaging of roughness dipoles can be applied over all four columns to obtain better converged statistics showing a clearer trend of streamwise variations.

Figure 8 shows the spanwise averaged r.m.s. values of roughness dipole sources for both the hemispherical and cuboidal fetches. Significant differences between hemispheres and cuboids are observed in terms of dipole strengths and distributions. First, the strengths of roughness dipoles approach constant values after approximately three rows for hemispheres and five rows for cuboids, indicating that the hemispherical fetch has a shorter entry region before acoustic statistics settle down. In terms of row-to-row variations, the lead row of hemispheres produces the weakest sound, the second row produces the strongest sound and the subsequent rows show a monotonic decrease leading to saturation in sound strength. In contrast, the cuboids show a monotonic decrease in sound strength except for the lead row of spanwise dipoles. Second, hemispherical dipoles are stronger in the spanwise direction than in the streamwise direction, which is consistent with the findings of Yang & Wang (2009) with a single hemisphere and a pair of hemispheres, whereas the opposite is true for cuboids. Finally, cuboids are much more efficient in generating sound than hemispheres. A comparison of dipole strengths in the fully developed region where streamwise variation is saturated reveals that cuboids produce sound that is approximately 5 dB louder than hemispheres. The underlying hydrodynamic causes for the above observations are explained in § 6.

https://doi.org/10.1017/jfm.2013.190 Published online by Cambridge University Press

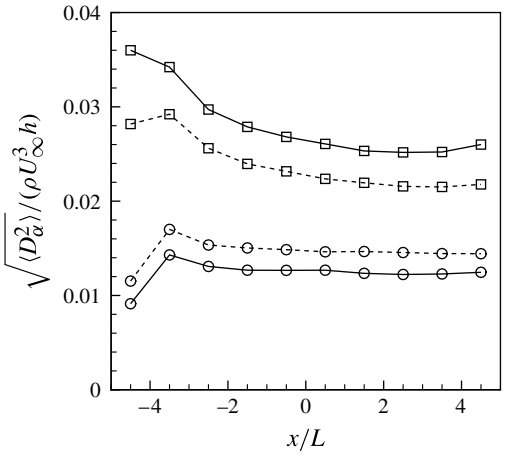


FIGURE 8. Root mean square of roughness dipole functions for hemispherical (○) and cuboidal (□) fetches averaged over all four columns. Each symbol corresponds to one row of roughness elements: ——, streamwise component; - - - -, spanwise component.

4.2. *Frequency spectra of roughness dipoles*

In the present work, the frequency content of a time-dependent function $F(t)$ is examined by its power spectral density (or spectrum) defined as

$$\Phi_{FF}(f) = \int_{-\infty}^{\infty} R_{FF}(\tau) \exp(-2\pi f \tau)\, \mathrm{d}\tau, \tag{4.1}$$

where $R_{FF}(\tau) = \langle F(t+\tau)F(t) \rangle$ is the autocorrelation function of $F(t)$ with τ denoting time separation and $\langle \cdot \rangle$ the time average.

Roughness dipole spectra also exhibit little variation among four elements in the same row, as shown in figure 9, which depicts the power spectral density of streamwise and spanwise dipoles of all four elements in the lead row and the eighth row of hemispherical and cuboidal fetches. Negligible spanwise variations are also observed for other flow and acoustic quantities associated with individual roughness elements, such as the roughness force strength and spectra, correlation and coherence between pairs of neighbouring elements, unsteady surface pressure distributions and their correlation and coherence with the roughness dipoles. Therefore, spanwise averaging can be performed over roughness dipole spectra for elements in the same row.

The streamwise variations of the spanwise-averaged power spectral density for select roughness rows are plotted in figure 10. For hemispheres, the first row shows a considerably lower spectral level than the rest in the mid-frequency range near the spectral peak, which is responsible for the lower r.m.s. dipoles strength shown in figures 7 and 8. The streamwise variation diminishes starting from the third row. For the cuboidal fetch, the streamwise dipole spectrum for the first row is at a higher level than the rest over all frequencies, which accounts for the highest r.m.s. dipole strength in figures 7 and 8. The spanwise dipole spectrum for the first row has a lower level at low frequencies and higher level at higher frequencies than the rest. It takes at least five rows before the spectral curves settle. This is again consistent with the behaviour of the roughness dipole strength shown in figure 8. Although the last rows see no downstream elements, their acoustic characteristics (see also dipole strengths

https://doi.org/10.1017/jfm.2013.190 Published online by Cambridge University Press

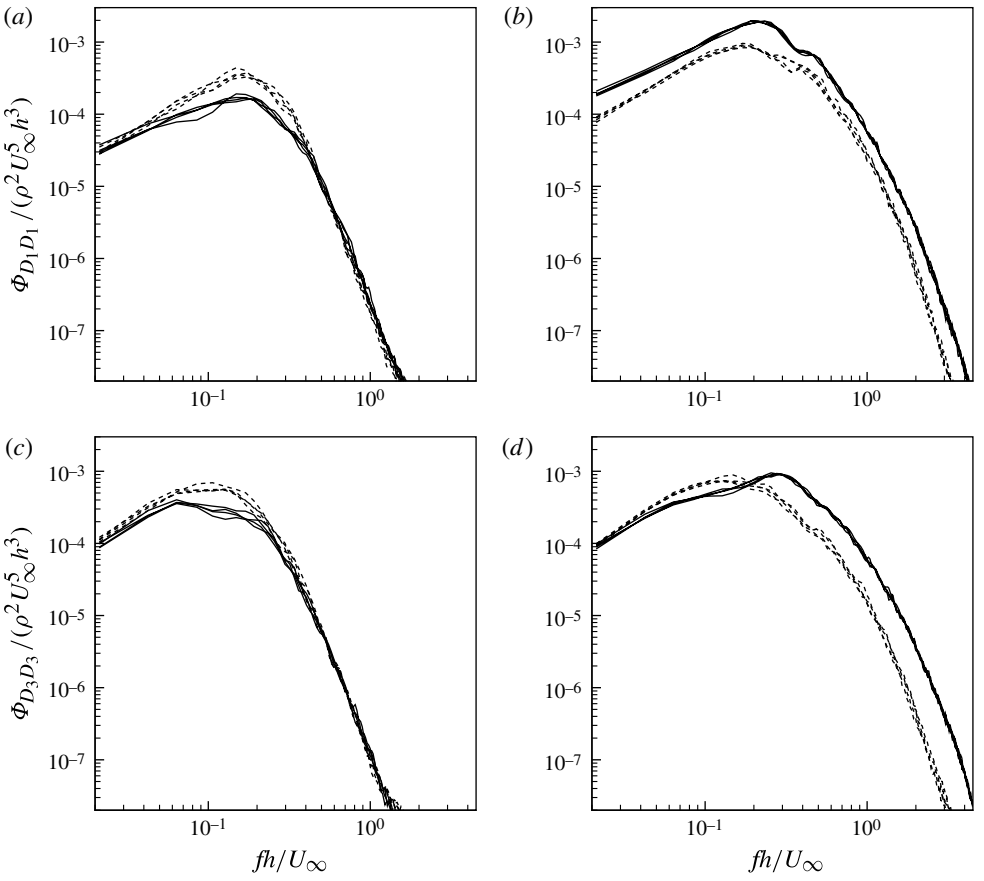


FIGURE 9. Power spectral density of (*a*) streamwise hemispherical dipoles, (*b*) streamwise cuboidal dipoles, (*c*) spanwise hemispherical dipoles and (d) spanwise cuboidal dipoles. Curves: ——, lead row; - - - -, 8th row.

in figure 8) are consistent with those of their upstream neighbours. This observation implies that the roughness dipole sound is not affected much by the downstream elements.

The near-collapse of spectral curves in the fully developed region suggests that a streamwise average, in addition to the spanwise average, can be performed to further improve statistical convergence in this region. Figure 11 shows the dipole spectra averaged over rows 6–9 and all four columns for both the hemispherical and cuboidal fetches. Overall, the roughness dipoles exhibit broadband characteristics, with cuboid dipoles containing much more high-frequency content. The streamwise dipoles for both types of elements show peak values at a common frequency of approximately $fh/U_\infty \approx 0.17$, which corresponds to a Strouhal number of $St = fh/U \approx 0.24$ based on a smooth-wall boundary-layer velocity of $U \approx 0.7U_\infty$ at the roughness height. For spanwise dipoles, the peak frequencies are slightly lower, with $St = fh/U \approx 0.15$ for hemispheres and 0.21 for cuboids. This figure also shows that hemispheres produce considerably lower sound levels than cuboids at all frequencies in the streamwise direction and at high frequencies in the spanwise direction. This is in qualitative agreement with experimental measurements of Alexander *et al.* (2010) with a single

https://doi.org/10.1017/jfm.2013.190 Published online by Cambridge University Press

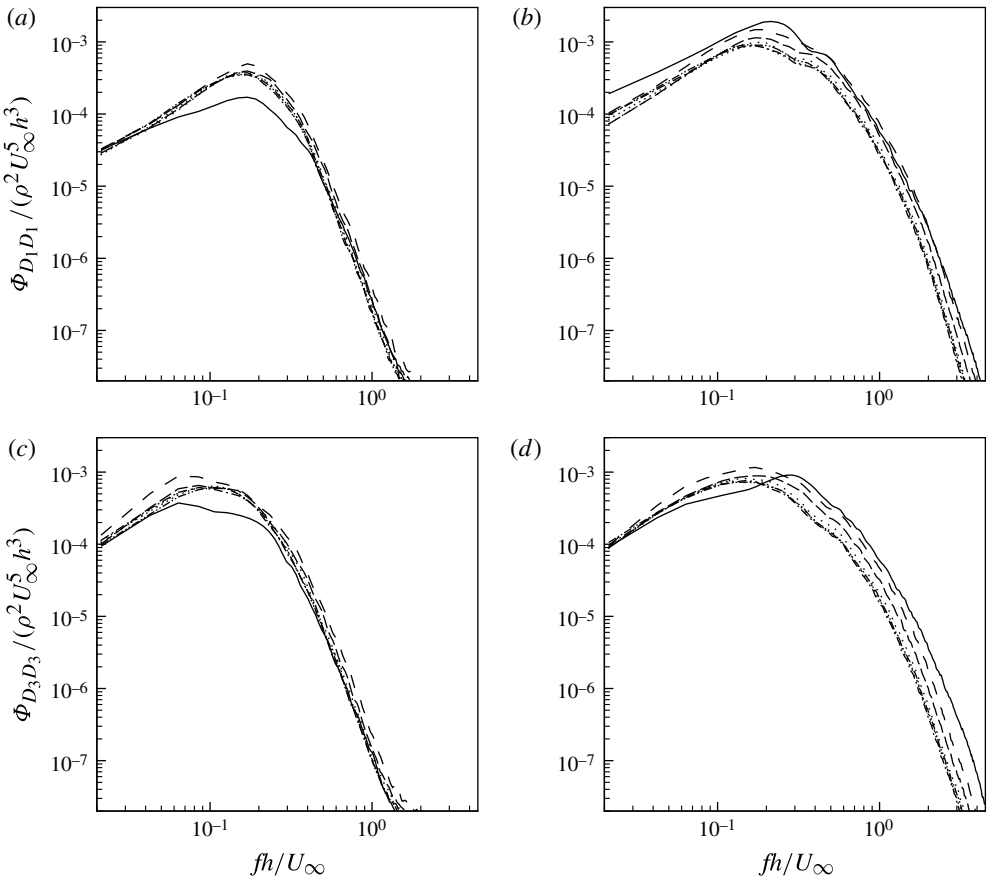


FIGURE 10. Column-wise averaged power spectral density of (*a*) streamwise hemispherical dipoles, (*b*) streamwise cuboidal dipoles, (*c*) spanwise hemispherical dipoles and (*d*) spanwise cuboidal dipoles. Curves: ——, 1st row; – – –, 2nd row; – – – –, 3rd row; · · · ·, 5th row; ·····, 7th row; —·—, 9th row; —··—, 10th row.

element and arrays of 7×6 elements. The low-frequency cuboid sound is comparable to hemisphere sound in the spanwise direction. The spanwise dipoles are stronger than streamwise dipoles at low to intermediate frequencies for hemispheres, as in the cases of single hemisphere and a pair of hemispheres (Yang & Wang 2009), whereas the two are of similar strength for cuboids. It is interesting to note that all of the dipole-source spectra show nearly the same frequency scaling ($\sim f^{1.3}$) at frequencies below their peak frequencies. At high frequencies, however, the spectral decay rate differs significantly for hemispheres and cuboids.

4.3. *Correlation and coherence between dipole sources*

To investigate the statistical dependence among discrete roughness dipoles, which affects the overall sound field, correlation coefficients and coherence between neighbouring streamwise and/or spanwise dipoles are examined. By definition, the time-correlation coefficient C and coherence γ^2 between any two dipoles $D_i^{(m)}$ and $D_j^{(n)}$

https://doi.org/10.1017/jfm.2013.190 Published online by Cambridge University Press

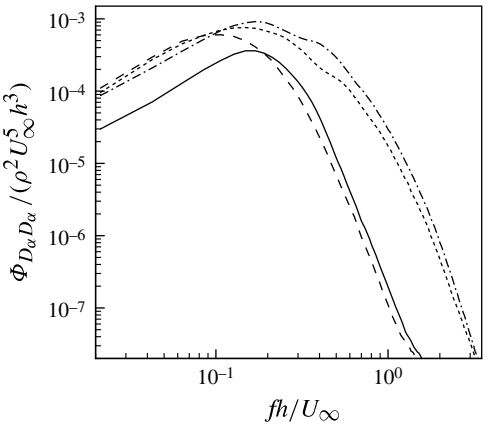


FIGURE 11. Power spectral density of roughness dipoles averaged over rows 6–9 and all four columns. Curves: ——, streamwise dipole for hemispheres; - - -, spanwise dipole for hemispheres; —·—, streamwise dipole for cuboids; ·····, spanwise dipole for cuboids.

are

$$C_{D_i^{(m)}D_j^{(n)}}(\tau) = \frac{\langle D_i^{(m)}(t) D_j^{(n)}(t+\tau)\rangle}{\langle D_i^{(m)2}(t)\rangle^{1/2}\langle D_i^{(n)2}(t)\rangle^{1/2}} \tag{4.2}$$

and

$$\gamma^2_{D_i^{(m)}D_j^{(n)}}(f) = \frac{|\Phi_{D_i^{(m)}D_j^{(n)}}|^2}{\Phi_{D_i^{(m)}D_i^{(m)}}\Phi_{D_j^{(n)}D_j^{(n)}}} \tag{4.3}$$

where the cross-spectral density $\Phi_{D_i^{(m)}D_j^{(n)}}(f)$ is calculated through a Fourier transform of the cross-correlation function $R_{D_i^{(m)}D_j^{(n)}}(\tau) = \langle D_i^{(m)}(t) D_j^{(n)}(t+\tau)\rangle$. In the following figures the superscripts (n) and subscripts i are dropped for convenience, and results are averaged across all four columns and rows 6–9 in the fully developed region for better statistical convergence.

Figures 12 and 13 show the averaged correlation coefficients and coherence between pairs of neighbouring streamwise or spanwise dipoles. Correlations and coherence between streamwise and spanwise components of neighbouring roughness dipoles are also calculated and found to be negligibly small. The results in the figures indicate that the overall correlations are small, with maximum values less than 0.17 for hemispheres and 0.07 for cuboids. For neighbouring dipoles aligned in the spanwise direction, the correlation and coherence are indistinguishable from statistical errors, further illustrating that there is little hydrodynamic interaction between roughness columns. But for neighbouring dipoles aligned in the streamwise direction, notable correlation peaks are observed for both hemispherical and cuboidal fetches at a time separation of $\tau U_\infty/L \approx 1.6$, which corresponds to a vortex convection speed of approximately $0.6U_\infty$. This observation implies that the interplay between roughness elements is mainly through wake convection; it is a one-way interaction between vortices shed from an upstream element and their downstream roughness element.

Although the correlation coefficients are generally small, their frequency decomposition shows that considerable coherence exists at low frequencies between

https://doi.org/10.1017/jfm.2013.190 Published online by Cambridge University Press

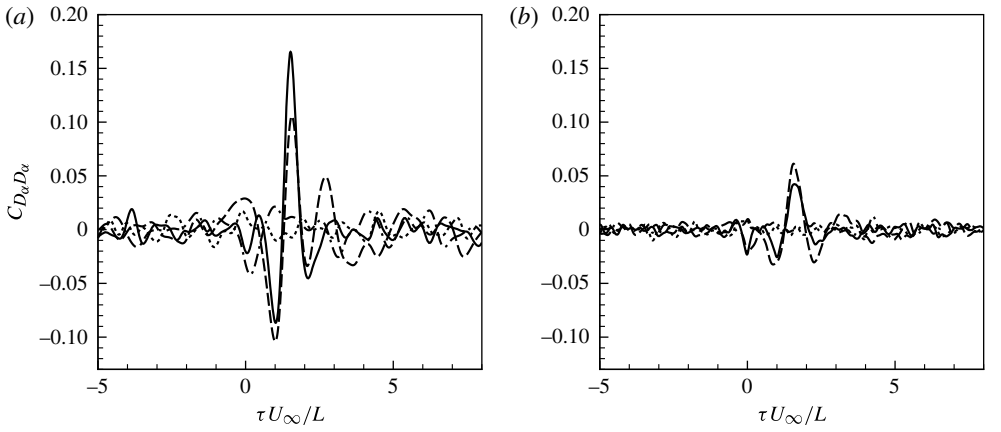


FIGURE 12. Correlations between neighbouring dipoles D_α in the fully developed region: (*a*) hemispherical fetch; (*b*) cuboidal fetch. Curves: ——, between streamwise neighbours of streamwise dipoles; ·····, between spanwise neighbours of streamwise dipoles; – – –, between streamwise neighbours of spanwise dipoles; —·—, between spanwise neighbours of spanwise dipoles.

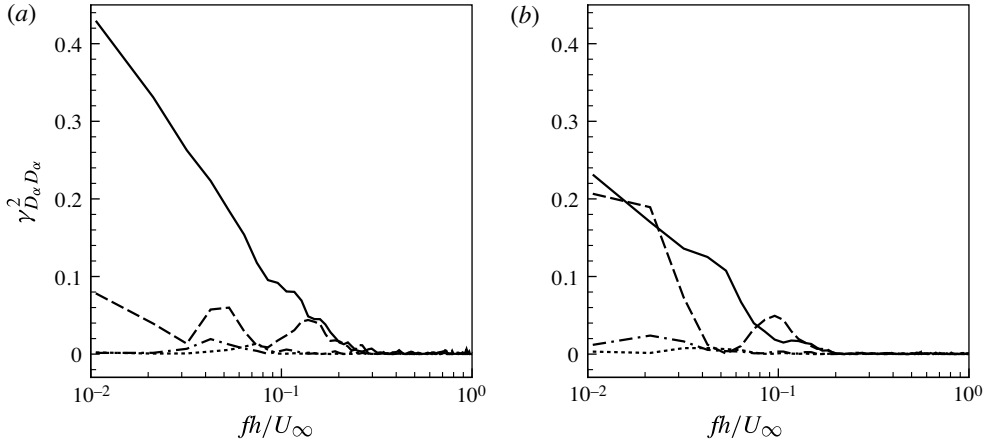


FIGURE 13. Coherence between neighbouring dipoles D_α in the fully developed region: (*a*) hemispherical fetch; (*b*) cuboidal fetch. Curves: ——, between streamwise neighbours of streamwise dipoles; ·····, between spanwise neighbours of streamwise dipoles; – – –, between streamwise neighbours of spanwise dipoles; —·—, between spanwise neighbours of spanwise dipoles.

neighbouring dipoles aligned in the streamwise direction, as illustrated in figure 13. These large coherence values do not contradict the small correlation coefficients because they occur at the low-frequency end where the dipole source spectra do not contain much energy. At the peak frequencies of roughness dipole spectra, the coherence levels are very low. The monotonic increase in streamwise coherence between streamwise dipoles with decreasing frequency indicates the increasing role of large-scale structures in the turbulent boundary layer in sound generation. These large eddies reside in the outer region of the boundary layer and are little affected

https://doi.org/10.1017/jfm.2013.190 Published online by Cambridge University Press

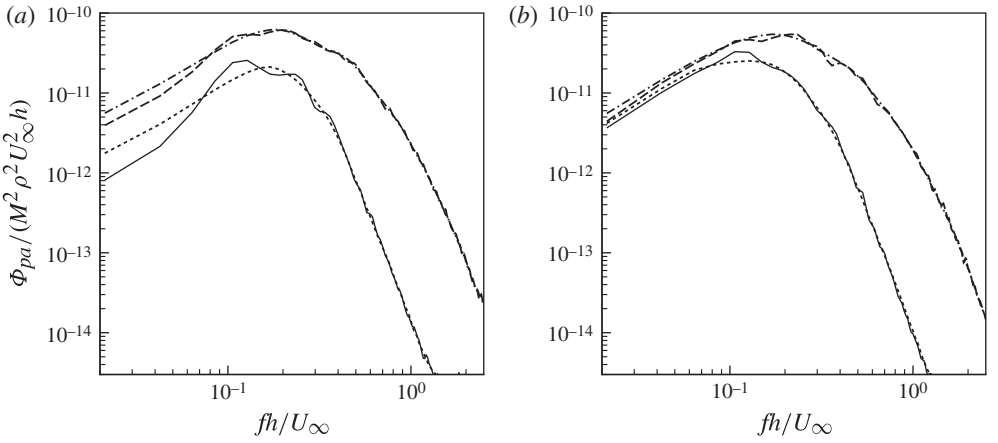


FIGURE 14. Sound pressure spectra at far-field locations: (*a*) $\boldsymbol{x}/L = (250\sqrt{2}, 250\sqrt{2}, 0)$ and (*b*) $\boldsymbol{x}/L = (0, 250\sqrt{2}, 250\sqrt{2})$. Curves: ——, sound from hemispherical fetch; - - - -, sound from cuboidal fetch; ·····, sum of sound spectra from individual hemispheres; —·—, sum of sound spectra from individual cuboids.

by the roughness elements, particularly the hemispheres. The multiple peaks in the streamwise coherence between neighbouring spanwise dipoles are not characteristic of boundary-layer turbulence and suggest that spanwise dipoles are more dominated by the coherent wake structures generated by the roughness elements even at low frequencies. The spanwise coherence between both streamwise and spanwise dipoles are very small at all frequencies, confirming little spanwise interaction in the entire frequency range.

Figure 14 shows the power spectral density of far-field acoustic pressure Φ_{pa} at two locations $\boldsymbol{x}/L = (250\sqrt{2}, 250\sqrt{2}, 0)$ and $(0, 250\sqrt{2}, 250\sqrt{2})$, both $500L$ away from the centre of the roughness fetch. The first location receives sound predominantly from the streamwise component of the roughness dipoles, and the second location receives sound predominantly from the spanwise dipoles. When calculating the far-field sound based on (2.1), no assumptions have been made regarding coherence among individual dipole sources, and interferences among sound waves emitted from different dipoles are accounted for accurately. The results are represented as solid and long-dashed lines for the two locations, respectively. In comparison, the far-field sound spectra calculated assuming statistically independent dipole sources (zero coherence), i.e. by summing up the spectra of sound from individual roughness elements are plotted as short-dashed and chain-dashed lines. The differences between the two results are significant at lower frequencies of $fh/U_\infty \leqslant 0.2$. This observation is consistent with figure 13 showing higher coherence between roughness dipoles for $fh/U_\infty \leqslant 0.2$.

5. Verification and validation

As indicated earlier, the simulation set-up and grid resolution in the present study follow those established by Yang & Wang (2009), where grid convergence of flow statistics was examined and extensive comparisons with experimental velocity and Reynolds stress profiles in the wake of a roughness element were made. Additional validation and verification of the current simulations are discussed in this section in terms of acoustic source spectra.

https://doi.org/10.1017/jfm.2013.190 Published online by Cambridge University Press

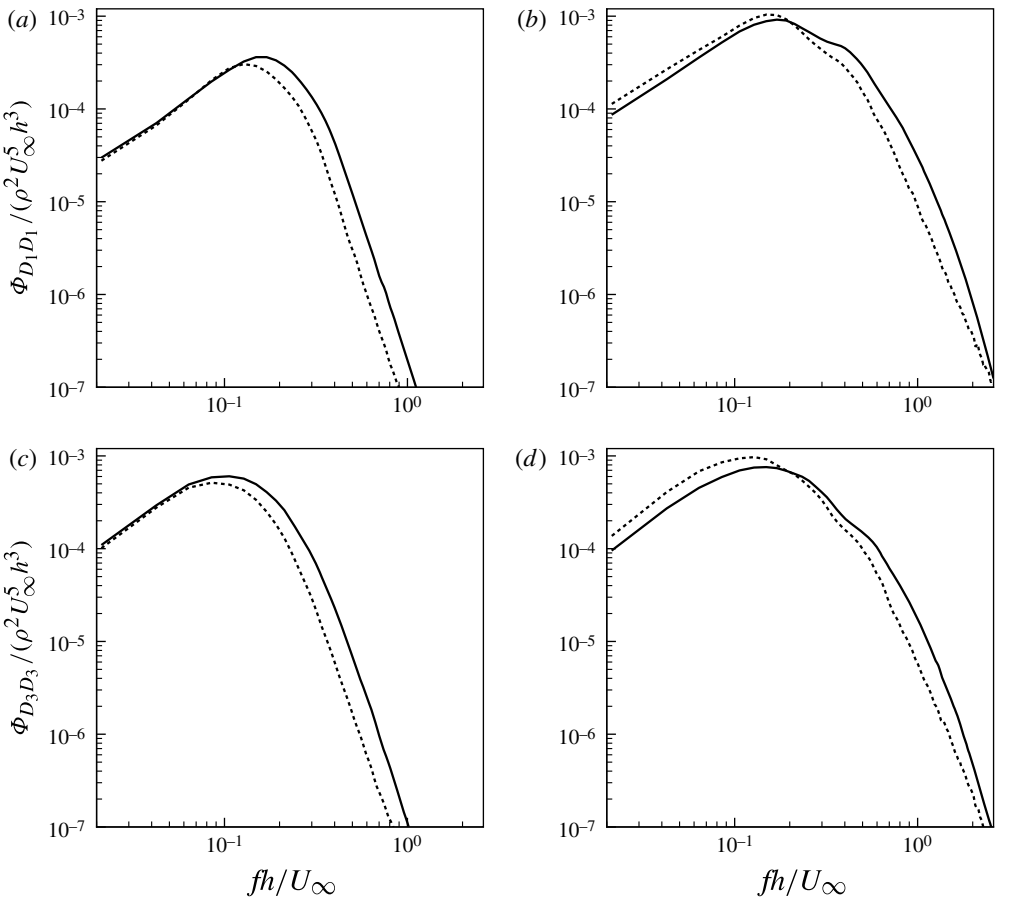


FIGURE 15. Power spectral density of (*a,b*) streamwise and (*c,d*) spanwise roughness dipoles in the fully developed region in (*a,c*) hemispherical and (*b,d*) cuboidal roughness fetches. Curves: ——, fine mesh with 40 million cells; - - - -, coarse mesh with 5 million cells.

To verify the computational results, a grid-resolution study was performed with an additional set of simulations in which the meshes were coarsened by a factor of two in each spatial direction. The coarsened meshes have approximately 5×10^6 cells, which is 1/8 the size of the original 4×10^7 cell meshes. The roughness dipole spectra in the fully developed regions are compared between fine-mesh and coarse-mesh solutions in figure 15. As expected, the main differences occur at high frequencies, with the coarse-mesh spectra declining sooner. At low frequencies, the coarse- and fine-mesh results match very well for hemispheres, and are only slightly off for cuboids (no more than 1.7 dB). The overall agreement is reasonable given the drastic difference in mesh sizes, and indicates validity of analysis based on the fine-mesh results.

To further assess the quality of computational results, a comparison is made with the experimental measurements of Alexander *et al.* (2011), as shown in figure 16. In the experiment, a least-squares analysis was used to estimate the spectra of 'source strengths', which are essentially the net forces exerted on an individual roughness

https://doi.org/10.1017/jfm.2013.190 Published online by Cambridge University Press

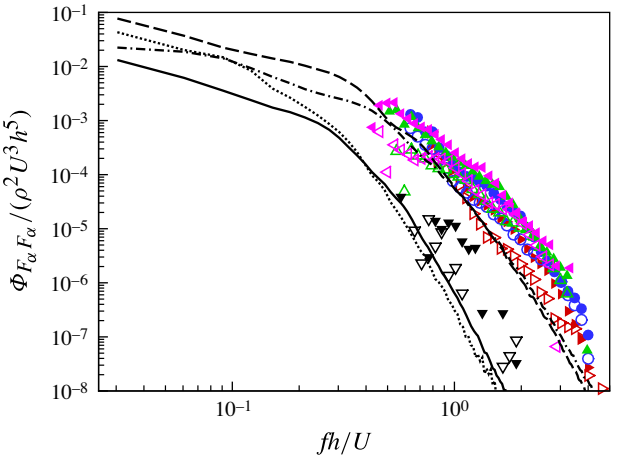


FIGURE 16. Spectra of roughness forces for single/lead-row roughness elements. Curves: computational results; symbols: experimental measurements by Alexander *et al.* (2011). Curves: ——, streamwise hemispherical forces; ·····, spanwise hemispherical force; – – –, streamwise cuboidal forces; —·—, spanwise cuboidal forces. Solid symbols: streamwise forces; open symbols: spanwise forces. ◁, single cube at $U_0 = 60$ m s^{-1}; △, single cube at $U_0 = 50$ m s^{-1}; ○, single cube at $U_0 = 40$ m s^{-1}; ▷, single cube at $U_0 = 30$ m s^{-1}; ▽, single hemisphere at $U_0 = 60$ m s^{-1}.

element by the flow as defined in (2.2). The comparisons are more qualitative than quantitative because of different flow configurations. The experiment was conducted in an anechoic wall-jet facility with a single roughness element (hemisphere or cube) of height $h = 3$ mm. The nozzle exit velocities in the experiment range from 20 to 60 m s^{-1}. The local boundary layer thicknesses are 21–16 mm, local maximum velocities U_m are 7.5–22 m s^{-1}, and the local velocity at the roughness height is $U = 0.8U_m$. Therefore under the experimental conditions, the local Reynolds number at roughness height is $Re_h = Uh/\nu = 1148$–3367. In the present boundary-layer computations, the local velocity at the roughness height is $U = 0.7U_\infty$ and the equivalent local Reynolds number is approximately $Re_h = Uh/\nu = 2740$, which falls within the experimental range. For consistency, the spectra and frequency are normalized using the respective local velocity U as the velocity scale. As discussed earlier, the strength of the roughness dipole from one element is not much influenced by its downstream or spanwise neighbours, and it is therefore reasonable to compare the lead-row roughness force spectra from computations with the single-element force spectra from the experiment. It is observed that the computational (lines) and experimental (symbols) spectra share similar shapes and levels. The computed spectral levels are in the lower range of experimental values and fall off faster than most experimental data, which may be related to grid resolution but differences in flow and roughness configurations may also be responsible. Note that reliable experimental data are available only at relatively high frequencies, where the computational results are less accurate. The computed spectra at lower frequencies are more accurate and provide an extension of the experimental data to the practically important lower-frequency range. In the frequency range where experimental data are available, they confirm the numerical predictions that cuboids are much stronger sound sources than

https://doi.org/10.1017/jfm.2013.190 Published online by Cambridge University Press

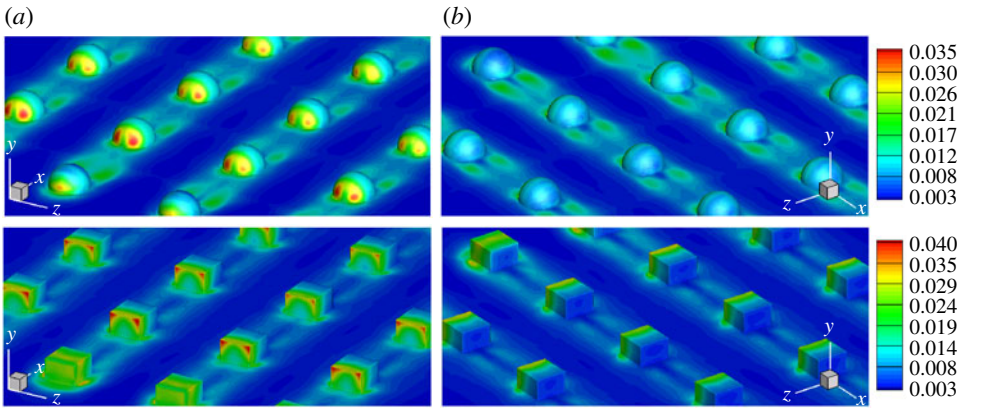


FIGURE 17. Isocontours of the r.m.s. values of surface pressure fluctuations $\langle p'^2\rangle^{1/2}/(\rho U_\infty^2)$ on portions of hemispherical and cuboidal roughness fetches with elements in rows 1–4 and all four columns: (*a*) viewed from upstream; (*b*) viewed from downstream.

hemispheres, and streamwise and spanwise forces are of similar magnitude in the frequency range compared.

6. Source mechanisms

6.1. *Surface pressure fluctuations*

Since roughness dipoles are directly related to the unsteady pressure on the surface of roughness elements through (2.2), the distribution of surface pressure fluctuations is indicative of important flow regions that contribute most to roughness sound radiation.

Figure 17 shows the r.m.s. values of pressure fluctuations on portions of the surfaces of roughness fetches including elements in rows 1–4 and all four columns. The distribution on the hemispherical fetch shows a single peak in the frontal area of each element in the first row resulting from the impingement of turbulent boundary-layer eddies, and two peaks in the frontal area of each element in subsequent rows due to the impingement of the unsteady wake. The back surfaces of hemispheres do not show significant pressure fluctuations. For the cuboidal fetch, intense pressure fluctuations also occur on the front surfaces rather than back surfaces of the elements, suggesting the importance of impinging flow structures rather than vortex shedding to sound generation. Distinctive impingement patterns between the lead row and subsequent rows are again observed. Moreover, the region with the most intense pressure fluctuations lies around the three frontal edges of each cuboid, where flow separation occurs. This implies that for cuboids, unsteady flow separation induced by sharp edges and the consequent reattachment play an important role in sound generation. This sharp-edge effect is most prominent for the lead row and decays gradually towards downstream, which shares the same trend as the streamwise distribution of cuboidal dipole strengths.

To relate pressure fluctuations to flow physics, composite plots of time-averaged streamlines and isocontours of the r.m.s. values of pressure fluctuations in planes $z = -0.5L$ and $y = h/2$ are plotted in figures 18 and 19, respectively. The streamlines show that as the flow approaches the roughness elements, it impinges on the frontal surface and forms small recirculation bubbles near the base of the elements, which is an indication of horseshoe vortices that are typical in junction flows (Simpson

https://doi.org/10.1017/jfm.2013.190 Published online by Cambridge University Press

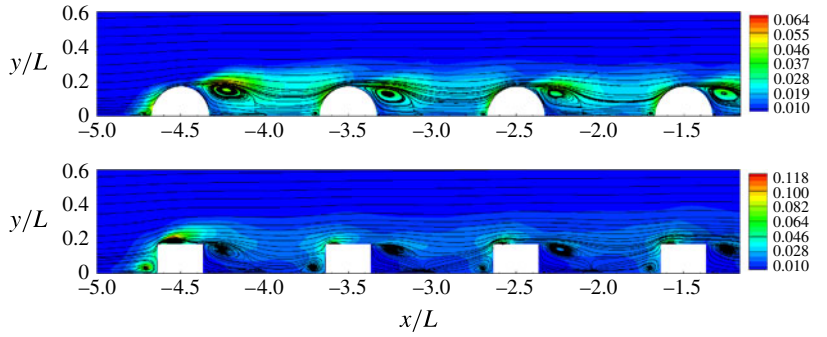


FIGURE 18. Time-averaged streamlines and isocontours of the r.m.s. values of pressure fluctuations $p'_{rms}(x, y)/(\rho U_\infty^2)$ in plane $z = -0.5L$ (cutting through centre of the second column of elements).

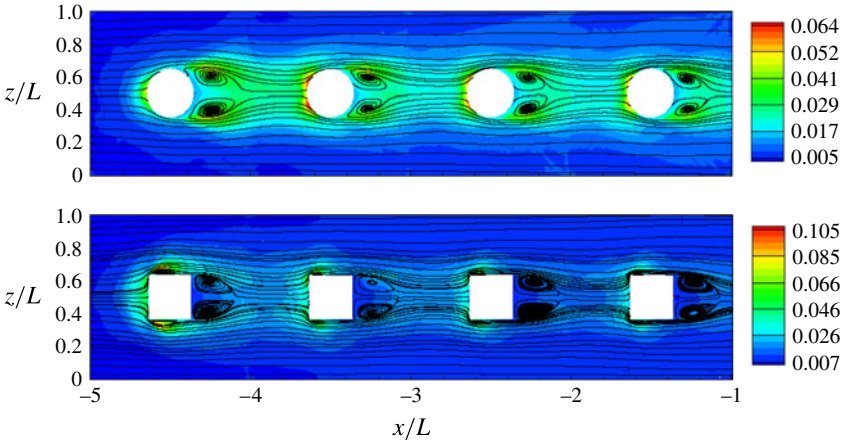


FIGURE 19. Time-averaged streamlines and isocontours of the r.m.s. values of pressure fluctuations $p'_{rms}(x, z)/(\rho U_\infty^2)$ in plane $y = h/2$ (cutting through half the roughness height) around the first four elements in the first column.

2001). However, coherent horseshoe vortices are only identifiable for the leading row of hemispherical elements as shown earlier in figure 5. For downstream elements that are immersed in turbulent wakes, horseshoe vortices lose their coherence and are only discernible in the time-averaged sense. The impingement of incoming turbulence and complex horseshoe vortices create large pressure fluctuations on the frontal surfaces of the hemispheres and cuboids. In the back of the roughness elements, flow separation creates a low-pressure-fluctuation zone on the back surfaces of the elements, while breakdown of the separated shear layers causes large pressure fluctuations away from the surfaces. For cuboids, the sharp frontal edges induce unsteady flow separation and strong pressure fluctuations in the vicinity of the separation bubbles. The edge-induced separation is stronger for the lead row than downstream rows, and causes unsteady side forces that are sources of spanwise dipoles.

The power spectral density of surface pressure fluctuations, calculated based on (4.1), is plotted in figures 20 and 21 for three frequencies to illustrate the variation

https://doi.org/10.1017/jfm.2013.190 Published online by Cambridge University Press

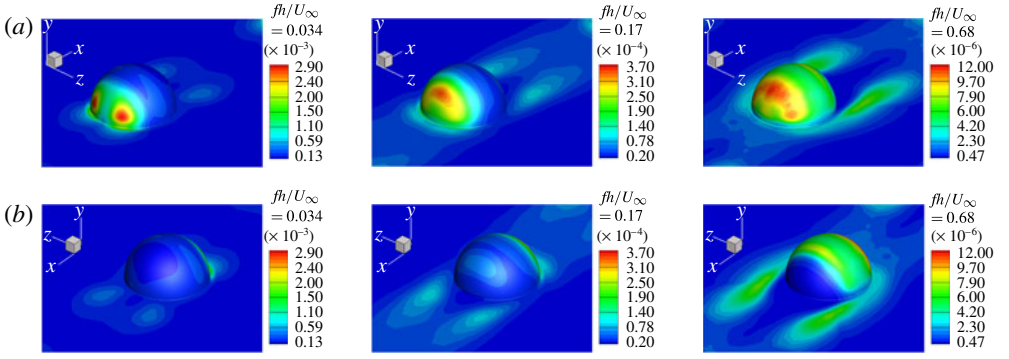


FIGURE 20. Isocontours of the power spectral density of pressure fluctuations $\Phi_{p'p'}(\boldsymbol{x}, f)/(\rho U_\infty^2)^2$ at select frequencies on and around a hemispherical roughness element in the fully developed region: (*a*) viewed from upstream; (*b*) viewed from downstream.

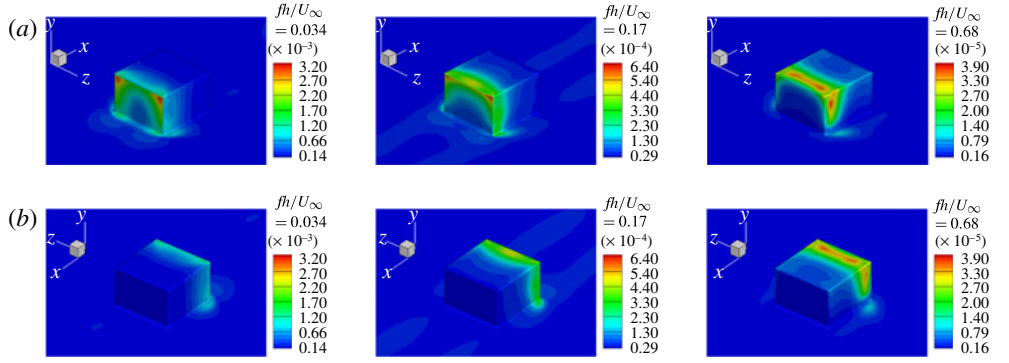


FIGURE 21. Isocontours of the power spectral density of pressure fluctuations $\Phi_{p'p'}(\boldsymbol{x}, f)/(\rho U_\infty^2)^2$ at select frequencies on and around a cuboidal roughness element in the fully developed region: (*a*) viewed from upstream; (*b*) viewed from downstream.

in spatial distribution of pressure fluctuation levels with frequency for both roughness types. The roughness element is in the fully developed region. At low frequencies, the high-intensity regions are more concentrated in the front and exhibit patterns that are consistent with the impingement of large-scale vortices shed from upstream elements. As the frequency increases, the high-intensity regions are more spread out towards the downstream portion of the surface, and the effect of self-generated structures, such as the unsteady separation along frontal edges of cuboids, becomes evident. This observation suggests that the impingement from upstream wakes are mainly responsible for lower-frequency surface pressure fluctuations, and the edge-induced structures produce mostly higher-frequency pressure fluctuations. At the peak sound frequency, both mechanisms are important in producing pressure fluctuations on the surface. On the back surface of the elements, the level of pressure fluctuations is low at all frequencies, again suggesting that shear-layer breakdown and vortex shedding in the wake are not significant noise sources for the element that produced them.

https://doi.org/10.1017/jfm.2013.190 Published online by Cambridge University Press

6.2. *Correlations of roughness dipoles with surface pressure fluctuations*

Additional physical insight into roughness noise source mechanisms, particularly with regard to the relative roles of diffraction and turbulence modification, can be gained by examining the correlation and coherence of surface pressure fluctuations with roughness dipoles and roughness forces. By definition, the correlation coefficient C and coherence γ^2 between a roughness dipole D_α and the surface pressure $p'(\Delta\boldsymbol{x}, t)$ are

$$C_{D_\alpha p'}(\Delta\boldsymbol{x}, \tau) = \frac{\langle D_\alpha(t)\ p'(\Delta\boldsymbol{x}, t+\tau)\rangle}{\langle D_\alpha^2(t)\rangle^{1/2}\ \langle p'^2(\Delta\boldsymbol{x}, t)\rangle^{1/2}} \tag{6.1}$$

and

$$\gamma^2_{D_\alpha p'}(\Delta\boldsymbol{x}, f) = \frac{|\Phi_{D_\alpha p'}(\Delta\boldsymbol{x}, f)|^2}{\Phi_{D_\alpha D_\alpha}(f)\ \Phi_{p'p'}(\Delta\boldsymbol{x}, f)}, \tag{6.2}$$

where $\Delta\boldsymbol{x}$ is the spatial separation between the pressure position and roughness dipoles whose locations are assumed to be concentrated at the geometric centres of the roughness elements projected onto the x–z plane. The cross-spectral density $\Phi_{D_\alpha p'}(\Delta\boldsymbol{x}, f)$ is calculated through a Fourier transform of the cross-correlation function $R_{D_\alpha p'}(\Delta\boldsymbol{x}, \tau) = \langle D_\alpha(t)\ p'(\Delta\boldsymbol{x}, t+\tau)\rangle$. Correlations and coherence are computed between roughness dipoles and pressure fluctuations in the surrounding area. To obtain better converged statistics, results are averaged over the two inner columns and rows 6–9 of roughness elements in the fully developed region.

In order to understand the effect of incoming turbulence on sound generation, correlation coefficients are calculated between streamwise dipoles $D_1(t)$ and surface pressure fluctuations $p'(x, t)$ along the centrelines across each column of roughness elements. Figure 22 shows this space–time correlation $C_{D_1 p'}(\Delta x, \tau)$ for the lead row and downstream rows in the fully developed region of both types of elements. For hemispheres, the streamwise dipole from the lead row is significantly correlated with pressure fluctuations over a long distance upstream, up to $\Delta x = -1.5L$. This indicates that the impingement of turbulent boundary-layer structures convected from upstream has a major effect on sound generation from the lead row of hemispherical patch. The correlation contours show a change in the convective behaviour close to the hemisphere as the near-wall turbulent eddies are distorted by the hemisphere. In contrast, the effect of upstream turbulence is significantly weaker for the cuboidal fetches, whose lead-row dipoles only show strong correlations with the pressure fluctuations on or around the element itself. This indicates that turbulence structures generated by the cuboids are mainly responsible for sound radiation. For downstream dipoles in the fully developed region, the incoming turbulence is dominated by wakes from upstream elements, and the wall-pressure correlations with streamwise dipoles are significant only within approximately $\Delta x = -0.6L$ for the hemispheres and $-0.5L$ for the cuboids, after reattachment of the shear layers from the upstream elements. The correlation patterns show lower convection velocities (smaller slopes) compared with those upstream of the lead row. The fluctuating wall pressure in the recirculation bubble behind the upstream element and further upstream are decorrelated with the dipoles. Overall, large-scale structures in the turbulent boundary layer do not have a major impact on roughness dipoles except for those in the lead rows and at very low frequencies.

It is noted from (2.2) that the dipole-source functions $D_\alpha(t)$ are the time derivatives of net unsteady forces $F_\alpha(t)$ on the roughness elements. Therefore, the cross-

https://doi.org/10.1017/jfm.2013.190 Published online by Cambridge University Press

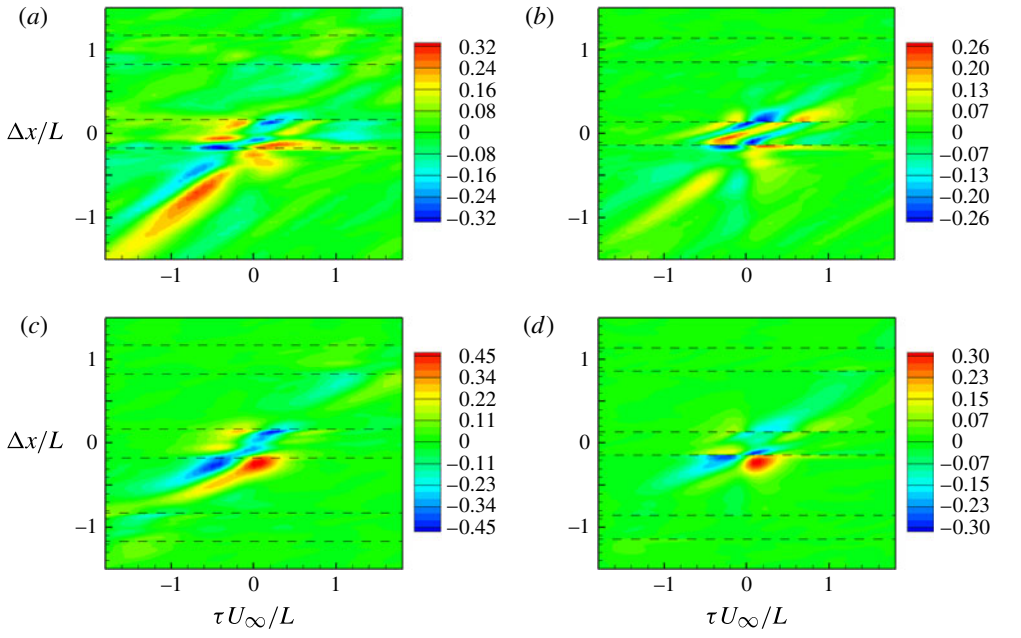


FIGURE 22. Isocontours of the correlation coefficients $C_{D_1p'}(\Delta x, \tau)$ between a streamwise dipole $D_1(t)$ and surface pressure fluctuations $p'(x, t)$ along the centreline across a column in hemispherical (*a,c*) and cuboidal (*b,d*) roughness fetches: (*a,b*) correlations with lead-row dipoles; (*c,d*) correlations with downstream dipoles in the saturated region. The dashed lines define the boundaries of roughness elements.

correlation of the dipole-source functions $D_\alpha(t)$ with surface pressure fluctuations is related to the cross-correlation of the forces $F_\alpha(t)$ with surface pressure fluctuations by

$$R_{D_\alpha p'}(\Delta \boldsymbol{x}, \tau) = -\frac{\mathrm{d}}{\mathrm{d}\tau} R_{F_\alpha p'}(\Delta \boldsymbol{x}, \tau). \tag{6.3}$$

As a consequence, the correlation coefficient $C_{F_\alpha p'}(\Delta \boldsymbol{x}, \tau)$ is the integral of $C_{D_\alpha p'}(\Delta \boldsymbol{x}, \tau)$ over τ multiplied by a factor of $-\langle D_\alpha^2(t)\rangle^{1/2}/\langle F_\alpha^2(t)\rangle^{1/2}$. Figure 23 shows $C_{F_\alpha p'}(\Delta \boldsymbol{x}, \tau)$ calculated in the same fashion as $C_{D_\alpha p'}(\Delta \boldsymbol{x}, \tau)$ and confirmed by this relationship. The force–pressure correlations exhibit a simpler pattern along the τ coordinate and a similar pattern along the Δx coordinates compared to the dipole–pressure correlations. The overall correlation levels are significantly higher than those for dipole–pressure correlations. Much longer time correlations are observed in the region immediately upstream of the roughness elements, which is due to stationary eddy structures in the area, such as the heads of horseshoe vortices. All forces correlate strongly with pressure fluctuations in the close upstream region, suggesting the importance of direct turbulence impingement and horseshoe vortices on roughness force generation. Convective patterns similar to those in figure 22, which are particularly prominent for the lead row, are observed, suggesting the role of diffraction of convected eddies in the generation of roughness forces and noise.

The coherence between roughness dipoles and surface pressure fluctuations provides information about the most relevant source regions at given frequencies. Based on (6.2)

https://doi.org/10.1017/jfm.2013.190 Published online by Cambridge University Press

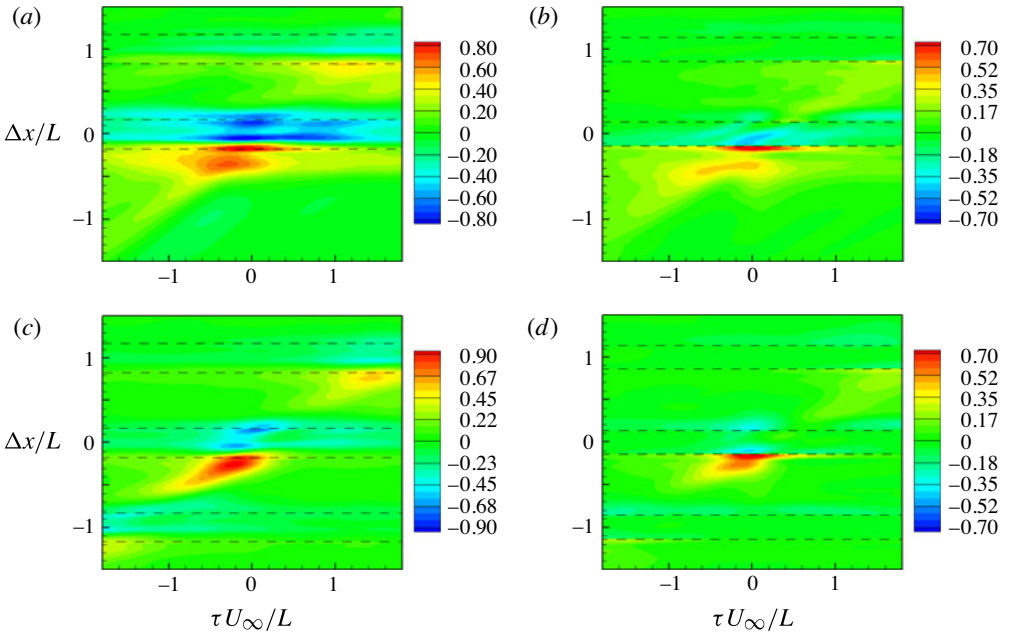


FIGURE 23. Isocontours of the correlation coefficients $C_{F_1p'}(\Delta x, \tau)$ between a streamwise force $F_1(t)$ and surface pressure fluctuations $p'(x, t)$ along the centreline across a column in the hemispherical (*a,c*) and cuboidal (*b,d*) roughness fetches: (*a,b*) correlations with lead-row forces; (*c,d*) correlations with downstream forces in the saturated regions. The dashed lines define boundaries of the roughness elements.

and (6.3), it can be shown that

$$\gamma^2_{D_{\alpha p'}}(\Delta \boldsymbol{x}, f) = \gamma^2_{F_{\alpha p'}}(\Delta \boldsymbol{x}, f), \tag{6.4}$$

i.e. the coherence between roughness dipoles and surface pressure fluctuations is identical to the coherence between roughness forces and surface pressure fluctuations. Therefore, it is only necessary to examine a single quantity.

Figures 24 and 25 show contours of the coherence of streamwise dipoles and spanwise dipoles, respectively, with the surface pressure fluctuations for both hemispherical and cuboidal elements in the fully developed region at three frequencies. The intermediate frequency $fh/U_\infty = 0.17$ corresponds to the peak frequency of the power spectral density of the streamwise dipoles. The dipoles exhibit high coherence with pressure fluctuations in relatively confined regions around the elements, which do not extend to any neighbouring elements, even at the lowest frequency considered. As the frequency increases, high coherence levels are more concentrated in smaller regions.

For streamwise dipoles associated with both hemispheres and cuboids, high-coherence regions on the flat surface in front of the elements persist for all frequencies shown, implying that the interaction of incoming turbulence with the frontal surface and horseshoe vortices play important roles throughout the frequency range. The coherence with pressure fluctuations on the back surfaces rises slightly as the frequency increases. However, considering that fluctuations on the back surfaces are much weaker than in the front, their contribution to sound generation is very small.

https://doi.org/10.1017/jfm.2013.190 Published online by Cambridge University Press

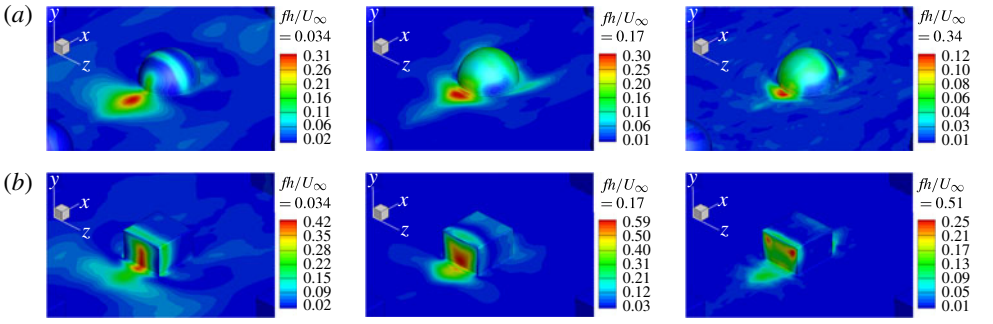


FIGURE 24. Isocontours of the coherence $\gamma^2_{D_1p'}(\Delta\boldsymbol{x}, f)$ between streamwise dipoles $D_1(t)$ and surface pressure fluctuations $p'(\Delta\boldsymbol{x}, t)$ in hemispherical and cuboidal roughness fetches at select frequencies f.

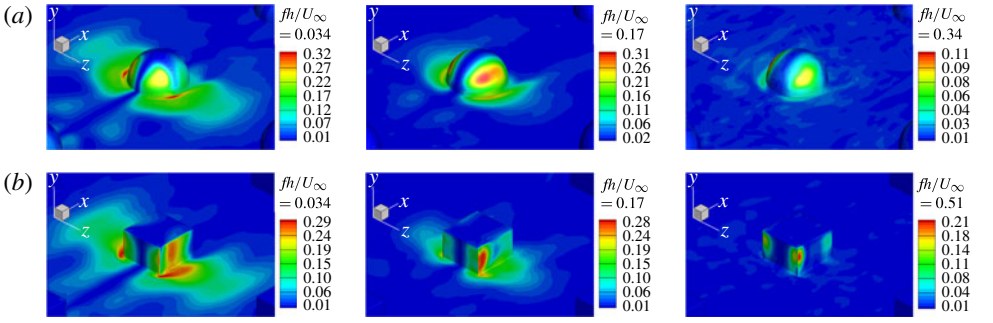


FIGURE 25. Isocontours of the coherence $\gamma^2_{D_3p'}(\Delta\boldsymbol{x}, f)$ between spanwise dipoles $D_3(t)$ and surface pressure fluctuations $p'(\Delta\boldsymbol{x}, t)$ in hemispherical and cuboidal roughness fetches at select frequencies f.

The spanwise dipoles for hemispheres are likewise most correlated with pressure fluctuations induced by horseshoe vortices around the frontal base and the impingement from the upstream wake at all frequencies. The spanwise dipoles for cuboids are most correlated with pressure fluctuations associated with flow separation and reattachment induced by the frontal edges and horseshoe vortices around the base at low frequencies. As the frequency increases, the role of horseshoe vortices decreases, and edge-induced flow separation produces the highest correlations between dipoles and surface pressure fluctuations.

6.3. *Space–time characteristics of unsteady surface pressure*

In addition to directly radiating sound as dipole sources, roughness elements induce elevated levels of pressure fluctuations on the wall, which can excite structural vibrations and additional noise radiation. The space–time characteristics of roughness-induced surface pressure fluctuations are therefore of interest in their own right and discussed briefly in this section.

To examine the effect of roughness elements on the space–time characteristics of surface pressure fluctuations, the space–time correlation coefficient $C_{p'p'}$ is calculated

https://doi.org/10.1017/jfm.2013.190 Published online by Cambridge University Press

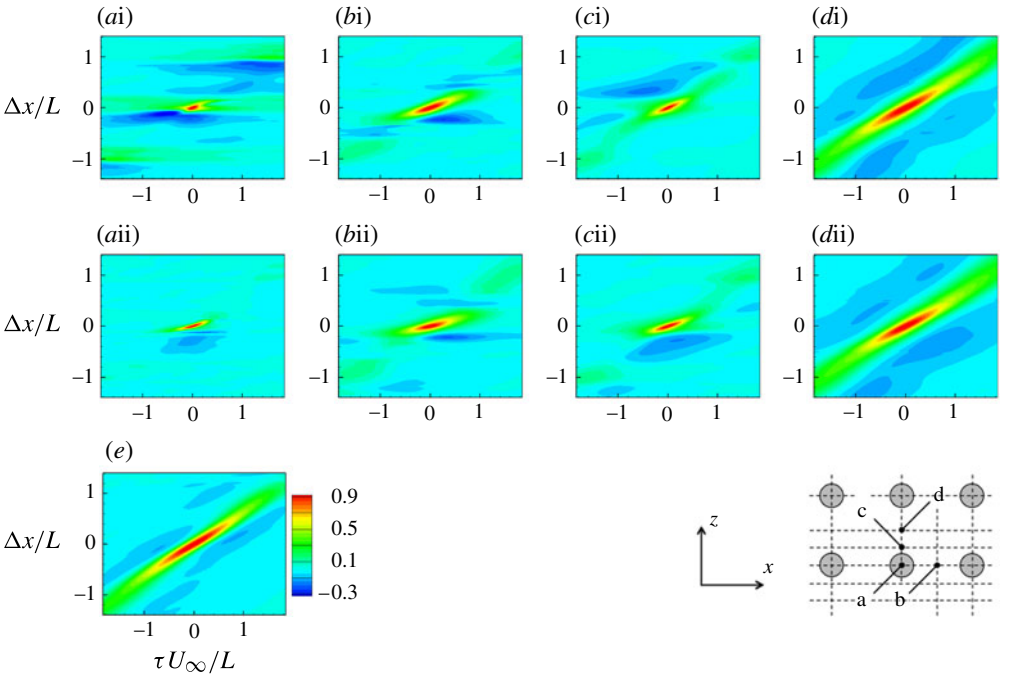


FIGURE 26. Space–time correlations of surface pressure fluctuations $C_{p'p'}(\boldsymbol{x}, \Delta x, \tau)$ with $\boldsymbol{x}$ at locations (a)–(d) depicted in the schematic for hemispherical (ai–di) and cuboidal ($a$ii–$d$ii) roughness fetches. Location (e) is in the unperturbed boundary layer upstream of the roughness fetch.

based on the following definition:

$$C_{p'p'}(\boldsymbol{x}, \Delta\boldsymbol{x}, \tau) = \frac{\langle p'(\boldsymbol{x}, t)p'(\boldsymbol{x} + \Delta\boldsymbol{x}, t + \tau)\rangle}{\langle p'^2(\boldsymbol{x}, t)\rangle^{1/2}\langle p'^2(\boldsymbol{x} + \Delta\boldsymbol{x}, t)\rangle^{1/2}}. \tag{6.5}$$

The results are illustrated in figure 26 as a function of temporal and streamwise spatial separations (τ and Δx) at four locations (a)–(d) around a roughness element as depicted in the schematic. The same quantity in the unperturbed boundary layer far upstream of the roughness fetch is also plotted as figure 26(e) for reference. At the centre top of the roughness element (location (a)), the streamwise correlation length is very small and limited to the size of the roughness element. These small-scale structures show a convective velocity (the slopes of the major axis of the oval-shaped, closed correlation contours) that is smaller than or comparable to that in the unperturbed boundary layer.

At the downstream location (b) between two neighbouring elements, which is close to the reattachment point for the separated shear layer from the upstream element, both temporal and streamwise scales grow larger, but decorrelations occur at the intersection with the roughness elements, and the local convection velocities are smaller than that in the unperturbed boundary layer. At locations (c) the correlation patterns are similar to those at location (b) with small differences in correlation times and lengths. At location (d), which is half-way between two elements in the spanwise direction and therefore least affected by the wakes of upstream elements, the patterns of correlation are convection dominated and similar to that in the unperturbed boundary layer,

https://doi.org/10.1017/jfm.2013.190 Published online by Cambridge University Press

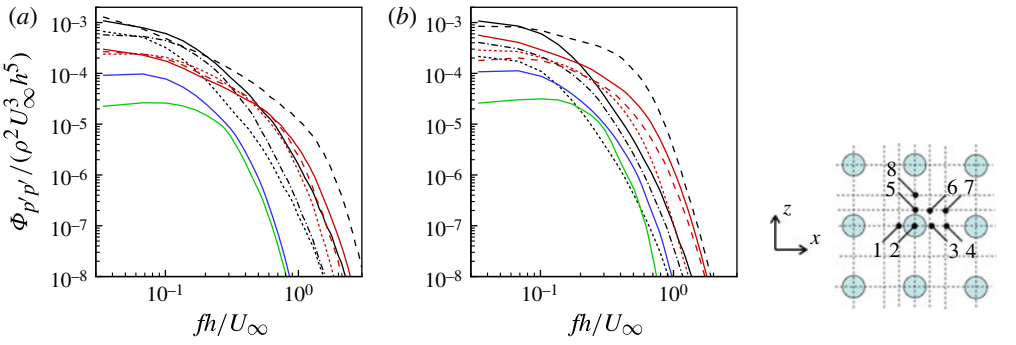


FIGURE 27. Power spectral density of surface pressure fluctuations $\Phi_{p'p'}(f)$ at locations surrounding a roughness element as labelled in the schematic for (*a*) hemispherical and (*b*) cuboidal roughness fetches. Curves: ——, location 1; - - - - -, location 2; ·····, location 3; —·—, location 4; red solid line, location 5; red long dashed line, location 6; red short dashed line, location 7; blue solid line, location 8; green solid line, unperturbed boundary layer.

with only a small increase in length and time scales. Traces of convection of large boundary-layer eddies (large streamwise and temporal separation) are visible in the correlation contours at other locations as well.

Figure 27 shows frequency spectra of pressure fluctuations at eight locations surrounding a roughness element in the fully developed region, as illustrated in the schematic. An additional location in the unperturbed boundary layer far upstream of the roughness fetch is used to provide reference values. It is observed that the surface-pressure-fluctuation spectra are elevated significantly over all frequencies in the roughness fetch in comparison to a smooth-wall boundary layer. The surface pressure fluctuations at location 1, which is directly in front of roughness elements, have the highest levels at low frequencies. At location 2, which is at the top centre of the element surface, the pressure fluctuations show highest levels at intermediate and high frequencies. Further downstream at locations 3 and 4, which are either within or near the edge of the recirculation bubbles, the pressure fluctuation levels are below the values at locations 1 and 2 but still significantly higher than the reference values. The differences between hemispherical and cuboidal fetches are significant at these two locations because of the different wake behaviour. Along the quarter lines between two columns at locations 5, 6 and 7, the variations in spectra are less dramatic and the maximum levels are lower than those along the centrelines of a column. Location 8 is most distant from any roughness element among all of the locations considered here, but the pressure fluctuation spectra are still significantly elevated relative to the reference spectrum.

7. Roughness fetch with short cylinders

In this section the roughness noise induced by an array of 10×4 short cylinders described in § 2 is discussed and compared with the noise from the hemispherical and cuboidal fetches.

Figure 28 shows the spanwise-averaged strength of cylindrical dipoles and their power spectral density averaged over rows 6–9, in comparison with the results for hemispherical and cuboidal roughness fetches. Similar to hemispherical dipoles, the cylindrical dipoles are stronger in the spanwise direction than in the streamwise

https://doi.org/10.1017/jfm.2013.190 Published online by Cambridge University Press

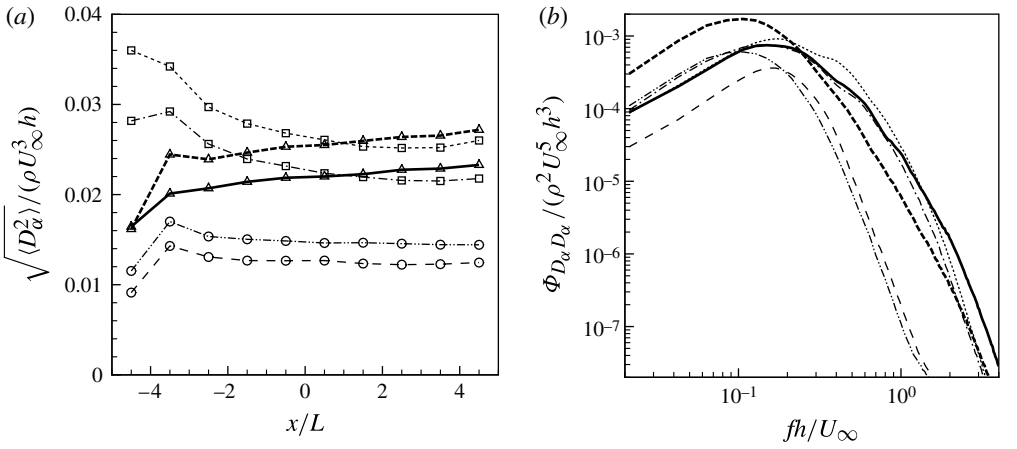


FIGURE 28. (a) Spanwise averaged r.m.s. of roughness dipoles and (b) their frequency spectra averaged over rows 6–9. Curves: ——, streamwise cylindrical dipoles; - - - - -, spanwise cylindrical dipoles; - - - -, streamwise hemispherical dipoles; —·—, spanwise hemispherical dipoles; ·····, streamwise cuboidal dipoles; —·—, spanwise cuboidal dipoles.

direction in terms of r.m.s. values. A spectral analysis shows that the stronger spanwise dipole lies in the lower-frequency range below the peak frequency for streamwise dipoles, whereas at higher frequencies the streamwise dipole is stronger. The dipole strength for the cylindrical fetch grows rapidly from the first to the second row, and then settles to a lower growth rate of 8–10 % from row 4 to row 10, but it does not reach a constant value within the 10 rows contained in the simulation. A longer roughness fetch is needed to allow flow and acoustics to become fully developed. The statistical averaging over rows 6–9 should therefore be interpreted as a local averaging to obtain smooth statistics. For the last four rows, cylindrical dipoles are even stronger than cuboidal dipoles, which makes cylinders the most efficient acoustic sources among the three roughness shapes considered, especially in the spanwise direction and at low frequencies. Interestingly, the cylindrical dipole shares the common peak frequency of $fh/U_\infty \approx 0.17$ in the streamwise direction with both hemispherical and cuboidal dipoles and $fh/U_\infty \approx 0.10$ in the spanwise direction with hemispherical dipoles. The correlation and coherence between neighbouring cylindrical dipoles are similar to those for hemispherical dipoles at slightly higher levels.

The distribution of surface pressure fluctuations in the cylindrical roughness fetch is illustrated in figure 29. Similar to the findings for hemispherical and cuboidal fetches, high levels of pressure fluctuations are found on the front half of the elements and show the effects of the impingement of upstream turbulence, flow separation and reattachment around the frontal sharp edge. The back surfaces of the cylinders again show very low level of pressure fluctuations, as a result of the shielding effect of the recirculation zones.

The coherence between cylindrical acoustic dipoles and surface pressure fluctuations are shown in figure 30 at three frequencies, among which the intermediate frequency is very close to the peak frequency for the dipole sources. The patterns of the coherence show a combination of effects of turbulence impingement, horseshoe vortices around the frontal base and edge-induced flow separation. At low frequencies, impinging turbulence and horseshoe vortices are better correlated with cylindrical dipoles

https://doi.org/10.1017/jfm.2013.190 Published online by Cambridge University Press

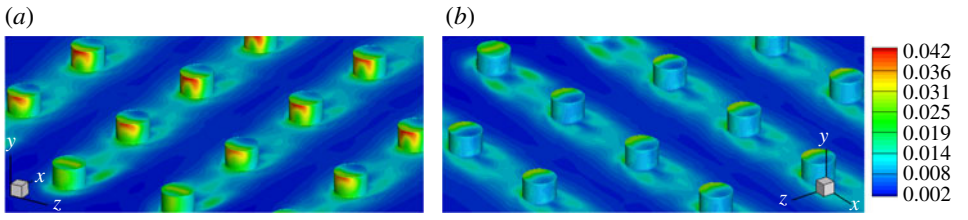


FIGURE 29. Isocontours of the r.m.s. values of pressure fluctuations $\langle p'^2\rangle^{1/2}/(\rho U_\infty^2)$ on a portion of the cylindrical roughness fetch with elements in rows 1–4 and all four columns: (*a*) viewed from upstream; (*b*) viewed from downstream.

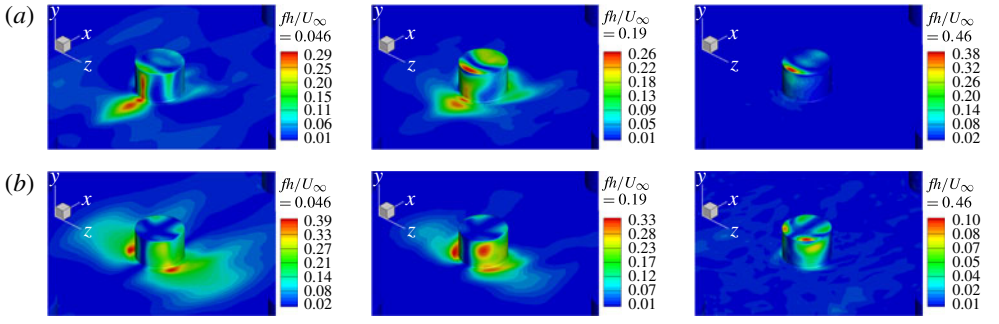


FIGURE 30. Isocontours of the coherence $\gamma^2_{D_\alpha p'}(\Delta\boldsymbol{x}, f)$ between streamwise dipoles $D_1(t)$ and surface pressure fluctuations $p'(\Delta\boldsymbol{x}, t)$ (*a*) and between spanwise dipoles $D_3(t)$ and surface pressure fluctuations $p'(\Delta\boldsymbol{x}, t)$ (*b*) for the cylindrical roughness fetch at select frequencies f.

than edge-induced separations, whose importance rises as the frequency increases. Compared with hemispheres and cuboids, cylinders possess certain geometric features of both, including a curved surface, a flat surface and a sharp edge. Therefore, the flow and acoustic characteristics of the cylindrical roughness fetch also share common features with hemispherical and cuboidal fetches.

8. Further discussion

Despite the relatively simple geometries and arrangements, the present analysis of the flow and acoustic fields associated with arrays of discrete roughness elements has generated significant new insight into the roughness-noise source mechanisms. The simulation results, together with earlier results for a single hemispherical element and two streamwise-aligned hemispherical elements (Yang & Wang 2009), can provide useful input to the development of noise prediction models at both conceptual and quantitative levels. Conceptually, the new understanding of acoustic source mechanisms can help identify physically important sources to model and eliminate unimportant noise sources. For example, vortex shedding from roughness elements used to be viewed as a dominant noise source and modelled in terms of bluff-body vortex shedding in a free stream (Smol'yakov 2001; Glegg *et al.* 2007). The computational results suggest, however, that vortex shedding is unimportant as a source of self-noise and should not be modelled as such, but its role in enhancing

https://doi.org/10.1017/jfm.2013.190 Published online by Cambridge University Press

near-wall turbulence and thereby the noise from downstream elements needs to be considered. The computational results also suggest, for the first time, that acoustic radiation in the spanwise direction is at least as strong as that in the streamwise direction and should therefore be included in any roughness noise model. The noise source processes are highly nonlinear, complex and shape-dependent, and thus a diffraction-theory-based model (e.g. Howe 1984, 1986) cannot be expected to produce accurate predictions in the fully rough regime. In quantitative terms, the simulations generated detailed data for unsteady forces, dipole source functions, flow statistics as well as correlations and coherence between dipole sources and between dipoles and fluctuating surface pressure. Many of these quantities are difficult to measure experimentally and thus particularly valuable for developing and calibrating theoretical models.

Roughness noise is a complex problem with a large parameter space. Even with regularly distributed roughness elements, the noise is affected by many geometric and flow parameters such as the roughness height, shape, density and Reynolds number. The preceding results are obtained with a fixed roughness height, distribution and Reynolds number. Because of the high computational expense it is not possible to explore the entire parameter space. Nonetheless, additional simulations have been performed in simpler configurations to assess the effects of two key parameters: the Reynolds number and roughness height. The primary objective is to determine if the preceding conclusions concerning acoustic properties and source mechanisms are of general significance with respect to changes in Reynolds number and roughness height. The results of these studies are documented by Yang (2012) and discussed briefly below.

The Reynolds-number effect is evaluated by conducting simulations at twice the previous momentum-thickness Reynolds number while the roughness height and spacing relative to the boundary-layer thickness are kept the same. The new Reynolds number at the inlet is $Re_\theta = 6130$, which corresponds to $Re_\tau = 2398$. Owing to the higher Reynolds number, the roughness height measured in wall units is increased to $h^+ = 308$. Hemispherical and cuboidal elements are considered, and computations are performed with a single column of 10 elements instead of 4 columns since negligible hydrodynamic and acoustic interactions exist among columns based on the roughness-array results. Despite the reduced number of elements and computational domain size, the computational mesh size is increased to approximately 5×10^7 cells for both types of elements in order to keep the grid resolution comparable to the lower-Reynolds-number cases in wall units. The simulation results confirm the same trends for relative source strengths and distributions as in the lower-Reynolds-number case. The streamwise variations of dipole strengths saturate more quickly because of stronger turbulent mixing, and the correlations and coherence between neighbouring dipole sources are slightly lower. The frequency spectra of dipole source functions averaged in the fully developed region (5th to 9th elements) are shown in figure 31 along with their lower-Reynolds-number counterparts. Higher-Reynolds-number flows generate more high-frequency content but lower spectral levels at low frequencies when scaled by U_∞^5, which is the perfect dipole scaling. The deviation is due to the highly nonlinear nature of the interstitial flow dynamics and their variation with h^+. Overall, all of the conclusions regarding relative source strengths, orientation, distribution and their geometric dependence drawn from the lower-Reynolds-number cases remain valid. Given that $Re_\theta = 6130$ is a significant Reynolds number and $h^+ = 308$ is deep in the logarithmic layer, it is reasonable to expect that these

https://doi.org/10.1017/jfm.2013.190 Published online by Cambridge University Press

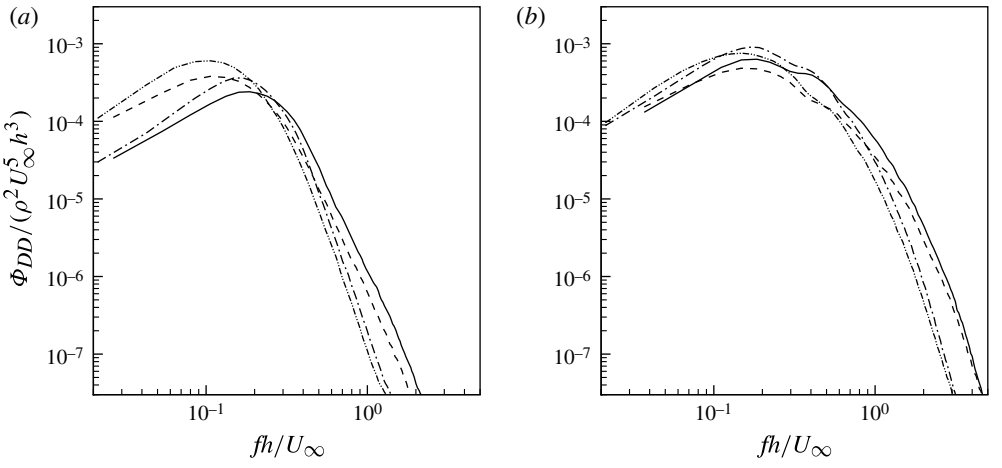


FIGURE 31. Power spectral density of (*a*) hemispherical and (*b*) cuboidal dipole source functions in the fully developed region. Curves: ——, streamwise dipole at $Re_\theta = 6130$; - - - -, spanwise dipole at $Re_\theta = 6130$; —·—, streamwise dipole at $Re_\theta = 3065$; —··—, spanwise dipole at $Re_\theta = 3065$.

conclusions will continue to hold at even higher Reynolds numbers in realistic applications.

The investigation into the roughness-height effect is performed with a fixed boundary-layer thickness and momentum-thickness Reynolds number. The simpler configuration of flow over two streamwise aligned hemispherical elements considered by Yang & Wang (2009), where $h = 0.036\delta$ ($h^+ = 95$), is used as the baseline case, and the roughness height is halved progressively to $h = 0.018\delta$ ($h^+ = 48$) and 0.009δ ($h^+ = 24$) in the new simulations while the centre-to-centre spacing is kept at $5.5h$. The Reynolds number at the inlet is $Re_\theta = 7500$ or $Re_\tau = 2666$. A comparison of the dipole source spectra is shown in figure 32. The source spectra associated with the two larger roughness heights are again in qualitative agreement with those associated with the first two rows of the hemispherical array in terms of the relative strengths between streamwise and spanwise dipoles and between the lead element and the downstream element, although the peak frequencies and strengths vary with h. The spectra for the smallest roughness height, on the other hand, show comparable peak levels between both dipole components and between both elements, because the hemispheres barely reach the logarithmic layer and induce only weak perturbations to the flow. The spectral levels show an approximate h^4 scaling, expected based on the surface area in (2.2), only for the streamwise dipoles at low frequencies. Variations are significant among spanwise dipoles and among streamwise dipoles at higher frequencies. An analysis of source mechanisms indicates that, similar to the hemispherical array case, the interactions of hemispheres with incoming turbulence and surround vortical structures are the dominant acoustic source for all three roughness heights. As expected, the dipole sources are better correlated with their neighbours and with upstream turbulence for smaller roughness sizes.

The limited parametric studies discussed in this section indicate that within the ranges examined, neither the roughness height nor the Reynolds number alters the conclusions of the roughness-array study in a fundamental way. Evidently, more investigations are needed to fully explore the parameter space and determine scaling

https://doi.org/10.1017/jfm.2013.190 Published online by Cambridge University Press

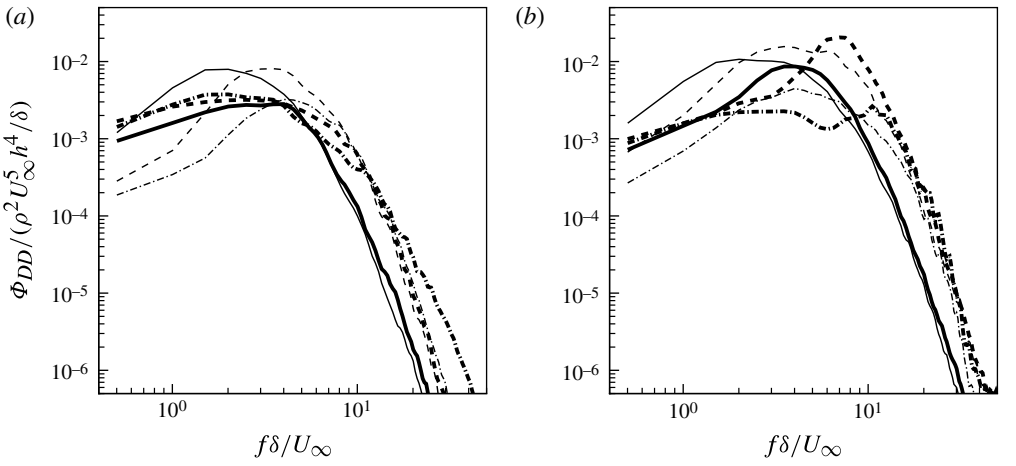


FIGURE 32. Power spectral density of dipole source functions associated with (*a*) upstream hemisphere and (*b*) downstream hemisphere in a turbulent boundary layer with two streamwise aligned hemispherical roughness elements: thick curves, streamwise dipoles; thin curves, spanwise dipoles. Curves: ——, $h^+ = 96$; - - - -, $h^+ = 48$; —·—, $h^+ = 24$. The Reynolds number at the inlet is $Re_\theta = 7500$.

relationships between roughness noise and key parameters. It should be noted that the present study only considers sparsely distributed roughness elements, which exhibit weak interactions among acoustic dipole sources. The level of interaction among roughness dipoles will increase if the elements are densely packed, which can alter the acoustic characteristics in a major way. In the experiment of Alexander *et al.* (2009), it is observed that the aerodynamic interaction between roughness elements does not have a large impact on the far-field sound unless the elements are packed so closely as to be in touch with one another. However, their conclusion is based on sound spectra at relatively high frequencies, where coherence levels are low and coherence lengths are very short. It will be of interest to examine numerically the aerodynamic interactions among densely distributed roughness elements and their impact on acoustics over a wide range of frequencies. In addition, future numerical investigations of roughness noise should also consider realistic, non-deterministic rough surfaces.

9. Conclusions

In this paper we have presented a computational study of roughness-induced noise in low-Mach-number turbulent boundary layers using LES and Lighthill's aeroacoustic theory. Simulations of turbulent boundary-layer flows over arrays of 10×4 sparsely distributed roughness elements have been carried out at $Re_\theta = 3065$, with roughness height equal to 0.124δ and element-to-element spacing equal to 0.727δ in both streamwise and spanwise directions. The roughness elements are acoustically compact and, together with their images in the plane wall, radiate sound predominantly as dipole sources in the plane of wall. The simulation results have been analysed to investigate the dipole source functions, their spatial and frequency distributions, and the underlying flow physics, with considerations of the roughness shape effect. A systematic statistical analysis, including correlations and coherence between roughness

https://doi.org/10.1017/jfm.2013.190 Published online by Cambridge University Press

dipoles and between dipole sources and surface pressure fluctuations, is conducted to elucidate the acoustic source mechanisms.

Three types of roughness elements, namely hemispheres, cuboids and short cylinders of the same height and flow blockage area, have been considered. For the roughness distributions considered, the spanwise variation among different columns in dipole source statistics is negligible, indicating little hydrodynamic interaction among the columns. The streamwise variation lasts 4–6 rows starting from the lead row for the hemispherical and cuboidal fetches before saturation, whereas for the cylindrical fetch a fully developed state is not reached by the 10th row. For the downstream elements in the fully developed region, cuboids emit sound that is approximately 5 dB louder than hemispheres. The sound radiated from downstream cylinders, even in the absence of saturation, is slightly stronger than that from cuboids.

For hemispherical roughness elements, the major conclusions from previous single- and double-hemisphere cases (Yang & Wang 2009) have been found to be valid for a roughness array as well. The dipole sources are mainly generated by the interaction of roughness elements with incoming turbulent eddies and surrounding vortical structures. Spanwise dipoles are stronger than streamwise dipoles at low and intermediate frequencies. Vortex shedding does not produce much self-noise, but it excites strong wake turbulence which enhances sound radiation from downstream elements. An examination of the dipole source distribution has revealed that the lead row of hemispheres in the roughness fetch produces the weakest sound, the second row produces the strongest sound and the rows further downstream produce sound of comparable intensity, which is significantly higher than that of the lead row.

For cuboids and cylinders, in addition to the impingement of incoming turbulence and vortical structures formed around the frontal base, unsteady flow separation induced by frontal sharp edges and the subsequent reattachment also provide significant sources of unsteady loading and dipole sound, particularly at relatively high frequencies. As a result, the dipole source distribution, orientation and frequency spectra exhibit strong dependence on the roughness shape. The cuboidal dipole sources show comparable strength in the streamwise and spanwise directions, more high-frequency content than hemispherical dipoles and stronger lead row than downstream rows. The cylindrical dipoles share features of both hemispherical and cuboidal dipoles. On the one hand, they are stronger in the spanwise direction and have a weaker lead row than downstream rows, as in the case of hemispherical dipoles. On the other hand, they contain a rich high-frequency content similar to cuboidal dipoles. As with hemispheres, the back surfaces of cuboidal and cylindrical elements experience weak pressure fluctuations and are therefore unimportant to sound generation.

The relative contribution of different source mechanisms to roughness sound also depends on the streamwise location of the roughness element. For the lead row, the impingement of boundary-layer eddies is the dominant source at low frequencies as evidenced by the long correlation and coherent distances between the dipole sources and upstream surface pressure fluctuations. For downstream rows, the boundary-layer eddies are less important relative to the turbulent wake structures generated by upstream elements.

Correlations and coherence among dipole sources associated with neighbouring roughness elements are found to be generally weak. There is little coherence between spanwise neighbours of roughness dipoles. The coherence between streamwise neighbours of dipole sources is also small except at low frequencies, indicating that the roughness elements act as independent acoustic sources over most frequencies.

https://doi.org/10.1017/jfm.2013.190 Published online by Cambridge University Press

Acknowledgements

This work was sponsored by the Office of Naval Research under Grant N00014-10-1-0452, with K.-H. Kim as program manager. Computer time was provided by the U.S. Department of Defense High Performance Computing Modernization Program through the Army Research Laboratory Supercomputing Resource Center and Naval Research Laboratory Affiliated Resource Center. We gratefully acknowledge William Blake, William Devenport and Stewart Glegg for valuable discussions. Portions of this work were presented in AIAA paper 2010-3772, 16th AIAA/CEAS Aeroacoustics Conference, Stockholm, Sweden, 7–9 June 2010 and AIAA paper 2011–2738, 17th AIAA/CEAS Aeroacoustics Conference, Portland, Oregon, 5–8 June 2011.

REFERENCES

ALEXANDER, W. N., DEVENPORT, W., GLEGG, S. A. L. & BUREN, R. V. 2010 Directivity of noise from discrete elements in a turbulent boundary layer. *AIAA Paper* 2010-3773.

ALEXANDER, W. N., DEVENPORT, W. & GLEGG, S. L. A. 2011 Aerodynamic noise from sparse surface roughness. *AIAA Paper* 2011-2740.

ALEXANDER, W. N., DEVENPORT, W. J. & GLEGG, S. L. A. 2013 Predictions of sound from rough wall boundary layers. *AIAA J.* **51**, 465–475.

ALEXANDER, W. N., RASNICK, M. B., CATLETT, M. R. & DEVENPORT, W. 2009 Boundary layer noise from discrete roughness elements. *AIAA Paper* 2009-3310.

ANDERSON, J., STEWART, D., GOODY, M., ZOCCOLA, P. & BLAKE, W. 2007 Sound from flow over a rough surface. *IMECE* 2007-41847.

BLAKE, W. K., KIM, K.-H., GOODY, M., WANG, M., DEVENPORT, W. & GLEGG, S. L. A. 2008 Investigations of roughness-generated TBL sound using coupled physical-computational experiments in conjunction with theoretical development. *Second ASA–EAA Joint Conference, Paris, France, July 2008*.

CHANAUD, R. C. 1969 Experimental study of aerodynamic sound from a rotating disk. *J. Acoust. Soc. Am.* **45**, 392–397.

COLE, L. D. 1980 Measurements of sound generated by boundary layer turbulence over smooth and rough surfaces. *Tech Rep.* SAD-288E-1942. David Taylor Naval Ship R&D Center.

CRIGHTON, D. G., DOWLING, A. P., FFOWCS WILLIAMS, J. E., HECKL, M. & LEPPINGTON, F. G. 1992 *Modern Methods in Analytical Acoustics,* Chapter 16. Springer.

CURLE, N. 1955 The influence of solid boundaries upon aerodynamic sound. *Proc. R. Soc. Lond. Ser.* A **231**, 505–514.

DEVENPORT, W. J., GRISSOM, D. L., ALEXANDER, W. N., SMITH, B. S. & GLEGG, S. A. L. 2011 Measurements of roughness noise. *J. Sound Vib.* **330**, 4250–4273.

DEVENPORT, W., WAHL, E. A., GLEGG, S. L. A., ALEXANDER, W. N. & GRISSOM, D. L. 2010 Measuring surface pressure with far field acoustics. *J. Sound Vib.* **329**, 3958–3971.

GLEGG, S. L. A. & DEVENPORT, W. 2009 The far-field sound from rough-wall boundary layers. *Proc. R. Soc. Lond.* A **465**, 1717–1734.

GLEGG, S. L. A., DEVENPORT, W. & GRISSOM, D. L. 2007 Rough wall boundary layer noise: Theoretical predictions. *AIAA Paper* 2007-3417.

GRISSOM, D. L., DEVENPORT, W. J. & GLEGG, S. L. A. 2007 Rough wall boundary layer noise: An experimental investigation. *AIAA Paper* 2007-3418.

GRISSOM, D. L., SMITH, B. & DEVENPORT, W. J. 2006 Rough wall boundary layer noise. *AIAA Paper* 2006-2409.

HERSH, A. S. 1983 Experimental investigation of surface roughness generated flow noise. *AIAA Paper* 1983-786.

HOWE, M. S. 1984 On the generation of sound by turbulent boundary layer flow over a rough wall. *Proc. R. Soc. Lond.* A **395**, 247–263.

HOWE, M. S. 1986 The influence of viscous surface stress on the production of sound by turbulent boundary layer flow over a rough wall. *J. Sound Vib.* **104**, 29–39.

https://doi.org/10.1017/jfm.2013.190 Published online by Cambridge University Press

HOWE, M. S. 1989 Sound produced by turbulent boundary layer flow over a finite region of wall roughness, and over a forward facing step. *J. Fluids Struct.* **3**, 83–96.

HOWE, M. S. 1998 *Acoustics of Fluid–Structure Interactions,* Chapter 3. Cambridge University Press.

HU, Z., MORFEY, C. L. & SANDHAM, N. D. 2006 Sound radiation from a turbulent boundary layer. *Phys. Fluids* **18**, 098101.

JI, M. & WANG, M. 2010 Sound generation by turbulent boundary-layer flow over small steps. *J. Fluid Mech.* **654**, 161–193.

JI, M. & WANG, M. 2012 Surface pressure fluctuations on steps immersed in turbulent boundary layers. *J. Fluid Mech.* **712**, 471–504.

LIGHTHILL, M. J. 1952 On sound generated aerodynamically. Part I. General theory. *Proc. R. Soc. Lond.* A **211**, 564–587.

LIU, Y. & DOWLING, A. P. 2007 Assessment of the contribution of surface roughness to airframe noise. *AIAA J.* **45**, 855–869.

LIU, Y., DOWLING, A. P. & SHIN, H.-C. 2006 Effects of surface roughness on airframe noise. *AIAA Paper* 2006-2510.

LIU, Y., DOWLING, A. P. & SHIN, H.-C. 2008 Measurement and simulation of surface roughness noise using phased microphone arrays. *J. Sound Vib.* **314**, 95–112.

LUND, T. S., WU, X. & SQUIRES, K. 1998 Generation of turbulent inflow data for spatially-developing boundary layer simulations. *J. Comput. Phys.* **140**, 233–258.

MAHESH, K., CONSTANTINESCU, G. & MOIN, P. 2004 A numerical method for large-eddy simulation in complex geometries. *J. Comput. Phys.* **197**, 215–240.

MORFEY, C. L. 2003 The role of viscosity in aerodynamic sound generation. *Intl J. Aeroacoust.* **2**, 225–240.

POWELL, A. 1960 Aerodynamic noise and the plane boundary. *J. Acoust. Soc. Am.* **32**, 982–990.

SHARIFF, K. & WANG, M. 2005 A numerical experiment to determine whether surface shear-stress fluctuations are a true sound source. *Phys. Fluids* **17**, 107105.

SIMPSON, R. L. 2001 Junction flows. *Annu. Rev. Fluid Mech.* **33**, 415–443.

SKUDRZYK, E. J. & HADDLE, G. P. 1960 Noise production in a turbulent boundary layer by smooth and rough surfaces. *J. Acoust. Soc. Am.* **32**, 19–34.

SMITH, B. S., ALEXANDER, W. N., DEVENPORT, W., GLEGG, S. L. A. & GRISSOM, D. L. 2008 The relationship between roughness noise and the near-field pressure spectrum. *AIAA Paper* 2008-2904.

SMOL'YAKOV, A. V. 2001 Noise of turbulent boundary layer flow over smooth and rough plates at low Mach numbers. *Acoust. Phys.* **47**, 218–225.

WANG, M., FREUND, J. B. & LELE, S. K. 2006 Computational prediction of flow-generated sound. *Annu. Rev. Fluid Mech.* **38**, 483–512.

YANG, Q. 2012 Computational study of sound generation by surface roughness in turbulent boundary layers. PhD thesis, University of Notre Dame, Notre Dame, Indiana.

YANG, Q. & WANG, M. 2008 Computational study of boundary-layer noise due to surface roughness. *AIAA Paper* 2008-2905.

YANG, Q. & WANG, M. 2009 Computational study of roughness-induced boundary-layer noise. *AIAA J.* **47**, 2417–2429.

YANG, Q. & WANG, M. 2010 Boundary-layer noise induced by a roughness patch. *AIAA Paper* 2010-3772.

YANG, Q. & WANG, M. 2011 Statistical analysis of acoustic-source field in rough-wall boundary layers. *AIAA Paper* 2011-2738.

https://doi.org/10.1017/jfm.2013.190 Published online by Cambridge University Press